PTB bericht
Wissenschaftliche Veröffentlichungen

Ex-16
Februar 2020

Habilitation

Holger Grosshans

Simulation of Turbulent Particle-laden Flows and their Electrostatic Charging

nw
ISSN 1868-5838
ISBN 978-3-95606-513-2

Physikalisch-Technische Bundesanstalt ■ Braunschweig und Berlin Nationales Metrologieinstitut

Physikalisch-Technische Bundesanstalt

Explosionsschutz
PTB-Ex-16
Braunschweig, Februar 2020

Holger Grosshans

Simulation of Turbulent Particle-laden Flows and their Electrostatic Charging

ISSN 1868-5838
ISBN 978-3-95606-513-2

https://doi.org/10.7795/110.20221208

Empfohlene Zitierweise/recommended citation
Grosshans, H., 2022. *Simulation of turbulent particle-laden flows and their electrostatic charging*.
Habilitationsschrift, Universität Magdeburg.
Braunschweig: Physikalisch-Technische Bundesanstalt. PTB-Bericht Ex-16.
ISBN 978-3-95606-513-2.
Verfügbar unter:
https://doi.org/10.7795/110.20221208

Herausgeber:
Physikalisch-Technische Bundesanstalt
ISNI: 0000 0001 2186 1887

Presse und Öffentlichkeitsarbeit

Bundesallee 100
38116 Braunschweig

Telefon: (05 31) 592-93 21
Telefax: (05 31) 592-92 92
www.ptb.de

Simulation of Turbulent Particle-laden Flows and their Electrostatic Charging

Habilitationsschrift

von Dr. tekn. Holger Grosshans

geb. am 21.10.1978 in Speyer

zur Verleihung des akademischen Grades

Doktor-Ingenieur habilitatus
(Dr.-Ing. habil.)

genehmigt von der Fakultät für Verfahrens- und Systemtechnik der Otto-von-Guericke-Universität Magdeburg am 3.3.2020.

Gutachter:
Prof. Dr.-Ing. habil. Ulrich Krause, Otto-von-Guericke-Universität Magdeburg
Prof. Dr. Uwe Klausmeyer, Technische Universität Braunschweig
Prof. Dr. Miltiadis V. Papalexandris, Université catholique de Louvain

https://doi.org/10.7795/110.20221208

Abstract

The dynamic motion of particles plays a prominent role in many naturally occurring flows as well as industrial applications. In this work, the author's efforts concerning the computation of a range of issues related to turbulent particle-laden flows are summarized. More specifically, the discussion of the research field starts with the numerical modeling of particle production through spray drying. This includes the simulation of a bi-component spray using the direct quadrature method of moments and the process of particle formation. Therein, the focus was given to the prediction of the drying kinetics and the resulting particle size and morphology. It was found that bi-component droplets dry qualitatively different whether they are exposed to temperatures below or above the boiling temperature of the involved liquid. Thus, a new model was proposed which accounts for the boiling of the liquid and possible cracking of the particle crust due to the resulting internal pressure increase.

The handling of the produced powder often leads to an accumulation of electrostatic charge which poses a hazard to the operational safety of plants. To gain insight into the charging, the author computed the pneumatic transport of particles through a wall-bounded turbulent carrier gas flow. A model was implemented, the so-called condenser model, to facilitate the prediction of the charge exchange between a particle and a solid surface during impact. This model was subsequently extended to enable the calculation of the important case of particles with non-conductive surfaces. The immobility of charge carriers leads to a non-uniform charge distribution on the particles' surface which was demonstrated to strongly affect its charging behavior during successive impacts. Afterward, large-eddy simulations were utilized to propose design parameters of transport pipes aiming to reduce the powder charge end to explore the dependency of the particles' properties on the charge accumulation. It was shown that the electric charge of the powder can be significantly decreased by reducing the conveying air velocity, the usage of larger pipes and the application of a higher solid mass flow rate. Also, the particles' mechanical and electrical properties represent promising measures to control the charge of the powder. As regards the mechanisms of charge transfer in fluid-solid mixtures, direct numerical simulations of channel flows revealed that charge may either be transported by convective motion or during inter-particle collisions. Finally, the studies of the author concerning the modulation of turbulent particle-laden duct flows under the influence of electrostatic charges are outlined. For the efficient and accurate calculation of the interaction between charged particles, a hybrid scheme that combines the advantages of both Gauss' and Coulomb's law was formulated. Utilizing this scheme, it was found that electrostatic forces tend to smooth the particle-concentration profiles over the duct cross-section. Also, the flow is stabilized which is expressed by the reduction of particle velocity fluctuations.

This summary aims to present the motivation for the conducted research, the fundamentals of the involved physics and the connections in-between the different works and the state-of-the-art. Also, the main results are discussed. Details concerning the mathematical models, numerical methods and discussions of the results are to be found in the respective publications.

Keywords: computational fluid dynamics, particle-laden flows, simulation, spray drying, electrostatics

https://doi.org/10.7795/110.20221208

Zusammenfassung

Die Dynamik von Partikeln spielt in vielen natürlich vorkommenden Strömungen sowie in industriellen Anwendungen eine bedeutende Rolle. Die vorliegende Arbeit fasst die numerischen Untersuchungen des Autors bezüglich turbulenter partikelbeladener Stömungen zusammen. Zunächst beginnt die Vorstellung der Forschung mit der numerischen Modellierung der Partikelproduktion durch Sprühtrocknung. Dazu gehört die Simulation eines Zweikomponentensprays mithilfe der Direct Quadrature Method of Moments und dem Prozess der Partikelbildung. Hierbei lag der Fokus auf der Vorhersage der Trocknungskinetik und der daraus resultierenden Partikelgröße und -morphologie. Es wurde festgestellt, dass Zweikomponententröpfchen qualitativ unterschiedlich trocknen, abhängig davon, ob sie Temperaturen unterhalb oder oberhalb der Siedetemperatur der jeweiligen Flüssigkeit ausgesetzt sind. Daher wurde ein neues Modell vorgeschlagen, dass das Sieden der Flüssigkeit und den möglichen Aufbruch der Partikelkruste aufgrund des erhöhten Innendrucks berücksichtigt.

Die Handhabung des erzeugten Pulvers führt häufig zu einer Akkumulation elektrostatischer Ladung, die die Betriebssicherheit von Anlagen gefährden kann. Um einen Einblick in den Aufladungsprozess zu erhalten, simulierte der Autor den pneumatischen Transport von Partikeln in einer wandnahen Strömung. Zur Vorhersage des Ladungsaustauschs zwischen einem Teilchen und einer festen Oberfläche während des Aufpralls wurde das sogenannte Kondensatormodell implementiert. Dieses Modell wurde anschließend erweitert, um die Berechnung des praxisrelevanten Falls von Partikeln mit nicht leitfähiger Oberfläche zu ermöglichen. Hier führt die Immobilität der Ladungsträger zu einer ungleichmäßigen Ladungsverteilung auf der Partikeloberfläche, von der gezeigt wurde, dass sie das Aufladeverhalten des Partikels stark beeinflusst. Anschließend wurden Grobstruktursimulationen durchgeführt, um Konstruktionsparameter für Transportrohre vorzuschlagen, die darauf abzielen, die Pulverladung zu reduzieren und um die Abhängigkeit der Aufladung von den Partikeleigenschaften zu untersuchen. Es wurde gezeigt, dass die elektrische Ladung des Pulvers durch Verringerung der Förderluftgeschwindigkeit, die Verwendung größerer Rohre und die Anwendung eines höheren Massendurchflusses deutlich verringert werden kann. Auch die mechanischen und elektrischen Eigenschaften der Partikel sind vielversprechende Maßnahmen, um die Ladung des Pulvers zu steuern. In Bezug auf die Mechanismen des Ladungstransfers in Fluid-Feststoff-Gemischen ergaben direkte numerische Simulationen von Kanalströmungen, dass Ladung entweder durch konvektive Bewegung oder während Kollisionen zwischen Partikeln transportiert wird. Abschließend werden die Studien des Autors über die Modulation turbulenter partikelbeladener Rohrströmungen unter Einfluss elektrostatischer Ladungen skizziert. Für die effiziente und genaue Berechnung der Wechselwirkung zwischen geladenen Teilchen wurde ein Hybridalgorithmus formuliert, der die Vorteile des Gauß'schen und des Coulomb'schen Gesetzes kombiniert. Bei Verwendung dieses Algorithmus wurde festgestellt, dass elektrostatische Kräfte dazu neigen, die Partikelkonzentrationsprofile über den Rohrquerschnitt zu glätten. Außerdem wird die Strömung stabilisiert, was sich in der Verringerung der Geschwindigkeitsschwankungen der Teilchen äußert.

Diese Zusammenfassung soll die Motivation für die durchgeführte Forschung, deren physikalische Grundlagen und die Verbindungen zwischen den verschiedenen Veröffentlichungen und dem aktuellen Stand der Wissenschaft darstellen. Außerdem werden die wichtigsten Ergebnisse diskutiert. Details zu den mathematischen Modellen, numerischen Methoden und den Ergebnissen sind in den jeweiligen Publikationen enthalten.

Schlagwörter: numerische Strömungsdynamik, partikelbeladene Strömungen, Simulation, Sprühtrocknung, Elektrostatik

Contents

1. Introduction 6
- 1.1. Motivation and organization of this document 6
- 1.2. List of summarized papers 6

2. Fundamentals of multiphase-EHD modeling 8
- 2.1. Fluid phase 8
  - 2.1.1. Navier-Stokes equations 8
  - 2.1.2. Turbulence, turbulent energy cascade and Kolmogorov hypotheses 8
  - 2.1.3. Turbulence modeling 10
- 2.2. Particulate phase 10
  - 2.2.1. Continuous and discrete description 10
  - 2.2.2. Forces on a particle 11
- 2.3. Electric field 12

3. Powder production 14
- 3.1. Introduction 14
- 3.2. Single droplet drying and particle formation [1, 2] 15
  - 3.2.1. Mathematical model 15
  - 3.2.2. Results and discussion 18
- 3.3. Spray drying [3, 4] 20
  - 3.3.1. DQMOM 20
  - 3.3.2. Results and discussion 21
- 3.4. Conclusions 24

4. Triboelectric particle charging [5] 25
- 4.1. Introduction 25
- 4.2. Particle charging models 26
  - 4.2.1. Condenser model 26
  - 4.2.2. Model of non-uniform particle charging 26
  - 4.2.3. Alternative theoretical concepts for particle charging 27
- 4.3. Results and discussion 28
- 4.4. Conclusions 30

5. Charging of fluid-solid mixtures 31
- 5.1. Introduction 31
- 5.2. Charge transport mechanisms 32
  - 5.2.1. Direct numerical simulations [6] 32
  - 5.2.2. Inter-particle charge diffusion [7] 34
- 5.3. Charge accumulation 36
  - 5.3.1. Pipe flows [8–10] 36
  - 5.3.2. Experimental investigations [11] 39
  - 5.3.3. Non-uniform particle charging [5] 39
  - 5.3.4. Electrostatic charging of helicopters in a dusty atmosphere [12, 13] 41
- 5.4. Conclusions 42

https://doi.org/10.7795/110.20221208

6. Flow modulation through electrostatic charges 43
6.1. Introduction 43
6.2. Interaction between charged particles 44
    6.2.1. Hybrid Gauss-Coulomb approach [14] 44
    6.2.2. Stochastic parcel model [15] 46
6.3. Emerging flow patterns [15, 16] 47
6.4. Conclusions 49

7. Perspectives 50

8. Bibliography 51

A. Author contribution statement 57

B. Acknowledgments 60

C. Curriculum Vitae 61

https://doi.org/10.7795/110.20221208

1. Introduction

1.1. Motivation and organization of this document

Particle-laden flows are of outstanding importance in manifold settings, both natural and man-made. As regards natural flows, examples that are shaping our world include sediment transport in coastal regions, dust storms or the reproduction of plants through the flight of pollen. Also in industrial applications, the specific behavior of particulates is often exploited e.g. in the form of pharmaceutical powders, powdered foods such as flour, milk or coffee, or fire extinguishing powder. Despite their widely different applications and characteristics, all fluid-solid mixtures have in common that the powder exhibits a large surface area. Thus, various microscopic processes occurring at the fluid-solid interface dominate the macroscopic behavior of the mixture. This wide range of scales of involved physical mechanisms forms a major obstacle to the theoretical description of particle-laden flows. A representative issue is the complex formation of particles in a spray drying device which is today mostly controlled based on empirical knowledge. However, its outcome in terms of particle size, shape and morphology is key to the usability of the resulting product. Also, the large surface area gives rise to triboelectric effects during the pneumatic transport of powder. Excessive charge accumulation leads to spontaneous spark discharges which resulted in the past in numerous dust explosions in industrial facilities.

This document aims to summarize the recent research efforts of the author concerning the two mentioned topics, namely powder production and electrification of particle-laden flows. The text presents the motivation of the various studies and gives the context of the main results to the scientific state-of-the-art. The body of the present document is organized as follows: Chapter 2 summarizes essential physics which serves as a basis for the contributions of the author given in the subsequent chapters. Chapter 3 presents the mathematical modeling of the production of powder through spray drying. Chapter 4 discusses the physics and theoretical considerations concerning the electrostatic charge exchange between a single particle and its surroundings. Chapter 5 outlines simulations regarding the charging of a complete powder. Chapter 6 elaborates on the modulation of the emerging flow pattern of turbulent particle-laden flows in case the particles carry a high charge. Finally, in chapter 7 unsolved questions are stated which deserve, according to the author's opinion, future research effort.

It is noted that the variables in this document are defined in a consistently manner and declared where they first appear. Thus, some variables may not be consistent with the published papers.

1.2. List of summarized papers

This document is based on the following publications whose contents have been updated and complemented:

[1] **H. Grosshans**, M. Griesing, M. Mönckedieck, T. Hellwig, B. Walther, S.R. Gopireddy, W. Pauer, H.-U. Moritz, N. Urbanetz, and E. Gutheil, *Numerical and experimental study of the drying of bi-component droplets under various drying conditions*, International Journal of Heat and Mass Transfer, 96, 97–109, May 2016

[2] **H. Grosshans**, M. Griesing, T. Hellwig, W. Pauer, H.-U. Moritz, and E. Gutheil, *A new model for the drying of mannitol-water droplets in hot air above the boiling temperature*, Powder Technology, 297, 259–265, April 2016

https://doi.org/10.7795/110.20221208

[3] **H. Grosshans**, S.R. Gopireddy, and E. Gutheil, *Numerical simulation of PVP-water sprays under various injection conditions*, 26th European Conference on Liquid Atomization and Spray Systems, ILASS – Europe 2014, September 8–10, 2014, Bremen, Germany

[4] **H. Grosshans**, S.R. Gopireddy, R.M. Humza, and E. Gutheil, *Modeling and simulation of single particle and spray drying of PVP- and mannitol-water in hot air*, in: Process-Spray: Functional Particles Produced in Spray Processes, Springer Science & Business Media, Springer, June 2016

[5] **H. Grosshans** and M.V. Papalexandris, *A model for the non-uniform contact charging of particles*, Powder Technology, 305, 518–527, January 2017

[6] **H. Grosshans** and M.V. Papalexandris, *Direct numerical simulation of the triboelectric charging in particle-laden turbulent channel flows*, Journal of Fluid Mechanics, 818, 465–491, March 2017

[7] **H. Grosshans** and M.V. Papalexandris, *Exploring the mechanism of inter-particle charge diffusion*, European Physical Journal Applied Physics, 82(1), 11101, 2018

[8] **H. Grosshans** and M.V. Papalexandris, *Large eddy simulation of triboelectric charging in pneumatic powder transport*, Powder Technology, 301, 1008–1015, July 2016

[9] **H. Grosshans** and M.V. Papalexandris, *Evaluation of the parameters influencing electrostatic charging of powder in a pipe flow*, Journal of Loss Prevention in the Process Industries, 43, 83–91, May 2016

[10] **H. Grosshans** and M.V. Papalexandris, *Numerical study of the influence of the powder and pipe properties on electrical charging during pneumatic conveying*, Powder Technology, 315, 227–235, April 2017

[11] N. Schwindt, U. von Pidoll, D. Markus, U. Klausmeyer, M.V. Papalexandris, and **H. Grosshans**, *Measurement of electrostatic charging during pneumatic conveying of powders*, Journal of Loss Prevention in the Process Industries, 49, 461–471, June 2017

[12] **H. Grosshans**, R.-Z. Szász, and M.V. Papalexandris, *Modeling the electrostatic charging of a helicopter during hovering flight in dusty atmosphere*, Aerospace Science and Technology, 64, 31–38, January 2017

[13] **H. Grosshans**, R.-Z. Szász, and M.V. Papalexandris, *Influence of the rotor configuration on the electrostatic charging of helicopters*, AIAA Journal, 56(1), 368–375, January 2018

[14] **H. Grosshans** and M.V. Papalexandris, *On the accuracy of the numerical computation of the electrostatic forces between charged particles*, Powder Technology, 322, 185–194, September 2017

[15] **H. Grosshans**, L. Villafañe, A. Banko, and M.V. Papalexandris, Case study on the influence of electrostatic charges on particle concentration in turbulent duct flows, *Powder Technology*, 357, 46–53, September 2019

[16] **H. Grosshans**, *Modulation of particle dynamics in dilute duct flows by electrostatic charges*, Physics of Fluids, 30(8), 083303, 2018

The author's contribution to these publications is stated in appendix A.

2. Fundamentals of multiphase-EHD modeling

In the following the fundamentals of the physics and mathematical modeling of the motion of fluids, particulates and electric fields are outlined. These formulations serve as the basis for the research presented in chapters 3–6 and may therein be reduced or extended to suit specific flow situations.

2.1. Fluid phase

2.1.1. Navier-Stokes equations

Strictly speaking, the Navier-Stokes equations name the momentum balance of incompressible Newtonian fluids. However, the term commonly refers to a set of equations governing the motion of general continuously deforming substances. Each of these equations is derived upon a fundamental physical principle of conservation of a certain quantity. With regard to the topics covered in the remainder of this document, the incompressible forms of the mass and momentum balance laws expressed in an Eulerian framework are given by

$$\nabla \cdot \boldsymbol{u} = 0 \tag{2.1a}$$

$$\frac{\partial \boldsymbol{u}}{\partial t} + (\boldsymbol{u} \cdot \nabla)\boldsymbol{u} = -\frac{1}{\rho}\nabla p + \nu \nabla^2 \boldsymbol{u} + \boldsymbol{F}_{\mathrm{s}}\,, \tag{2.1b}$$

where $\boldsymbol{u}$ denotes the fluid's velocity, p the pressure, ρ the density, ν the kinematic viscosity, and t the temporal coordinate. Further, in case of the simultaneous presence of another phase, e.g. dispersed solid or liquid, the source term $\boldsymbol{F}_{\mathrm{s}}$ accounts for the momentum transfer between the particles, respectively droplets, and the carrier fluid. Mass conservation relies on the assumption that mass can neither be created nor destroyed, while the momentum conservation equation extends Newton's second law of motion to fluids. Since analytical solutions are so far only available for few simplified flow cases, the solution of the above equations requires the application of numerical approximations.

2.1.2. Turbulence, turbulent energy cascade and Kolmogorov hypotheses

In 1883, Osborne Reynolds conducted a classical experiment injecting a dye in the center of a pipe flow to visualize a streakline. He revealed that the flow characteristics is fully described by a single dimensionless number, consequently called Reynolds number, Re, defined as

$$Re = \frac{UL}{\nu}\,, \tag{2.2}$$

where U and L are representative velocity and length scales. For low values of Re the streakline showed to be straight and undisturbed only blurred due to molecular diffusion, which corresponds to the features of a *laminar* flow. When the fluid velocity was increased the streakline started to fluctuate in an irregular manner indicating a *transitional* flow. Finally, for high Reynolds numbers, the flow became *turbulent*, i.e., exhibiting a random, dissipative, diffusive, irregular and three-dimensional behavior.

As regards turbulent flows, Lewis Fry Richardson promoted in 1922 the idea of an *energy cascade* [17]. According to it, turbulence is composed of eddies of various characteristic length-,

https://doi.org/10.7795/110.20221208

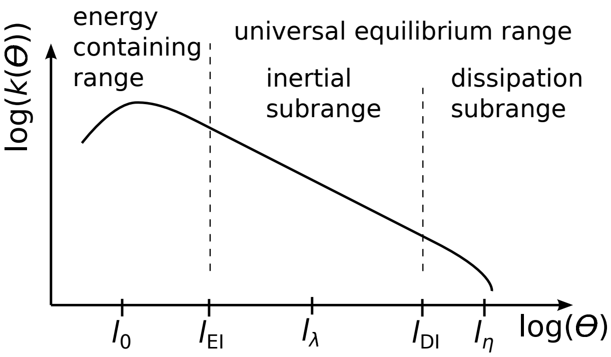

Figure 2.1.: Turbulent kinetic energy (k) spectrum of a turbulent flow as a function of the wave number Θ.

velocity-, and timescales, denoted by l, u, and τ, respectively. Further, turbulent kinetic energy is assumed to be produced on the large scales of fluid motion for which the effects of viscosity are small compared to inertial effects. Thus, these eddies are unstable and break up into smaller structures which in turn break up into even smaller ones until their size is sufficiently small whereby viscosity becomes important. Finally, eddies of the smallest scale dissipate which inhibits the accumulation of turbulent structures of small sizes. It is noted that while in average turbulent energy is transferred from large to small scales, locally and intermittently the transfer can act in the opposite direction. The latter is referred to as backscatter which can be of a significant amount in certain situations [18]. A schematics of the energy content of fully developed turbulence as a function of the wave number is depicted in figure 2.1.

In 1941, Andrei Nikolajewitsch Kolmogorov contributed to the picture of the energy cascade by postulating three hypotheses. More precisely, he argued that the eddies of the largest scale, l_0, also called *integral length scale*, are affected by the geometry of the flow domain. However, the resulting anisotropy diminishes when eddies break up on their way down the energy cascade. As a conclusion, he formulated the *hypothesis of local isotropy* [19]:

> At sufficiently high Reynolds numbers, the small-scale turbulent motions ($l \ll l_0$) are statistically isotropic.

Further, Kolmogorov defined the length scale l_{EI} which distinguishes between a range of anisotropic and a range of isotropic eddies. The flow scales larger than l_{EI} are referred to as *energy-containing range*. For the isotropic eddies Kolmogorov stated the *similarity hypothesis* [19]:

> In every turbulent flow at sufficiently high Reynolds numbers, the statistics of the small-scale motions ($l < l_{\mathrm{EI}}$) have a universal form that is uniquely determined by ν and the turbulent dissipation rate, ε.

Consequently, the flow scales smaller than l_{EI} are called the *universal equilibrium range*. This range is further divided by l_{DI} which marks the border between the *inertial* and the *dissipation subrange*. The former contains those eddies whose motions are affected only by inertia whereas the dynamics of the latter depend additionally on dissipation. Thus, Kolmogorov stated concerning the inertial subrange another *similarity hypothesis* [19]:

> In every turbulent flow at sufficiently high Reynolds numbers, the statistics of the motions of scale l in the range $l_0 \gg l \gg l_\eta$ have a universal form that is uniquely determined by ε and independent of ν.

One may theoretically quantify some scales of turbulent motion which are relevant for the modeling concepts in the following section. In particular, the *Taylor scale* [20],

$$l_\lambda / l_0 \sim Re_{\mathrm{T}}^{-1/2}, \tag{2.3}$$

https://doi.org/10.7795/110.20221208

is located in the inertial subrange. In the above equation, Re_T represents the turbulence Reynolds number which is based on the size and velocity of the integral turbulent scales. Further, the size of the smallest eddies in a turbulent flow field, called *Kolmogorov scale eddies*, can be estimated through dimensional analysis and Kolmogorov's hypothesis as

$$l_\eta = \left(\frac{\nu^3}{\varepsilon}\right)^{1/4} \qquad \text{or} \qquad l_\eta / l_0 \sim Re_\mathrm{T}^{-3/4} . \tag{2.4}$$

2.1.3. Turbulence modeling

The resolution of all length- and time-scales of fluid motion on a numerical grid, termed *direct numerical simulation* (DNS), represents the most exact method to simulate turbulence. However, from equation (2.4) it becomes evident that turbulent flows of a high Reynolds number exhibit a wide range of scales which results in a challenging task in terms of computational effort. Thus, DNS is limited to generic domains and low Reynolds number flows and not feasible for the simulation of industrial-scale applications. Therefore, techniques have been developed to model turbulence instead of resolving it.

According to the *large eddy simulation* (LES) methodology, a filter is applied to the governing equations (2.1a) and (2.1b) and only the turbulent structures larger than the filter size are resolved on the grid. This choice relaxes the requirements for the spatial resolution significantly compared to DNS. However, through the filter operation, new unclosed terms corresponding to the small (sub-filter) scales appear. Since the filtering is often realized implicitly by the numerical grid, these terms are also referred to as sub-grid-scale (SGS) terms.

The rationale of the LES methodology stems from Kolmogorov's hypothesis that the small-scale structures are universal which facilitates their modeling. Suitable modeling of the related terms has been the subject of research for several decades. Some of the most popular closures include those by Smagorinsky [21], the dynamic approach by Germano et al. [22] and the scale similarity model by Bardina et al. [23]. Nonetheless, all of them suffer from certain deficiencies, most notably the assumption of the correlation between the filtered rate of strain and the sub-filter terms which were proven through experiments to be weak [24]. An alternative forms the implicit approach by Boris et al. [25]. Therein, dissipation at the small scales is effectuated, instead of through an explicit SGS model, by the properties of the employed numerical schemes. However, one may rely on such a model only if the grid resolution is fine enough so that a considerable part of the turbulence energy spectrum is resolved.

A further reduction of the computational effort is accomplished by temporal or ensemble averaging of the governing equations which leads to the *Reynolds-averaged Navier-Stokes* (RANS) equations. This is often a reasonable approach as for many real-scale flows only time-averaged quantities are of interest and not their turbulent fluctuations. However, similar to the filtering operation in LES, due to the averaging new unclosed terms arise which are referred to as *Reynolds stresses*. The modeling of these terms, especially in the near-wall region, causes the major impairment of RANS simulations. Popular closures include the mixing-length model of Baldwin and Lomax [26] and the standard $k-\varepsilon$ [27] and $k-\omega$ [28] models.

2.2. Particulate phase

2.2.1. Continuous and discrete description

A range of complementary computational approaches is available to describe a dispersed particulate phase. They can be distinguished in methods describing the particulate phase in the Eulerian or Lagrangian framework.

https://doi.org/10.7795/110.20221208

In the Eulerian framework the particulate phase is considered to behave as a continuum characterized by the particle number density function,

$$\zeta = \zeta(\boldsymbol{u}_\mathrm{p}, r_\mathrm{p}, Q; \boldsymbol{x}, t)\,. \tag{2.5}$$

This expression gives the probable number density of particles at time instance t located at $\boldsymbol{x}$ having a velocity of $\boldsymbol{u}_\mathrm{p}$, a radius of r_p, and carrying an electrical charge of Q. The evolution of ζ reads, analogous to Williams' spray equation [29] for droplets and to Boltzmann's equation for molecules,

$$\frac{\partial \zeta}{\partial t} + \frac{\partial(\boldsymbol{u}_\mathrm{p}\zeta)}{\partial \boldsymbol{x}} = -\frac{\partial(\sum \boldsymbol{f}\,\zeta)}{\partial \boldsymbol{u}_\mathrm{p}} - \frac{\partial(\dot{Q}\,\zeta)}{\partial Q}\,. \tag{2.6}$$

The first term on the right-hand side of the above equation represents the sum of the external forces affecting ζ whereas $\dot{Q}$ denotes the change of the particle charge. Eulerian approaches require the existence of unique field representations for the properties of the particulate phase. This assumption restricts implicitly the maximum Stokes, St, and Knudsen, Kn, numbers that can be considered. The Stokes number is defined as the ratio between the particle response time τ_r and the characteristic time-scale of the fluid flow, τ_f, i.e.,

$$St = \tau_\mathrm{r}/\tau_\mathrm{f}\,. \tag{2.7}$$

A particle of a small Stokes number follows the flow closely whereas the trajectories of particles of a high Stokes number are hardly influenced by the surrounding fluid. The Knudsen number, on the other hand, is the ratio of the average particle spacing to a characteristic flow time scale. Thus, particulates of a low Kn tend to reach a local equilibrium due to frequent inter-particle collisions.

In the Lagrangian framework, each particle is treated individually as a point-mass whose motion is computed as

$$\frac{\mathrm{d}\boldsymbol{u}_\mathrm{p}}{\mathrm{d}t} = \sum \boldsymbol{f}\,, \tag{2.8}$$

where $\boldsymbol{u}_\mathrm{p}$ is the velocity of the given particle. The term on the right-hand side of the above equation represents the sum of all specific external forces acting on the particle which are elaborated in the following sub-section. The advantage of the Lagrangian approach is that there is no limitation on St and polydispersity can be handled more easily compared to the Eulerian approach. However, the ratio of the average particle diameter to the characteristic flow scale is assumed to be low. Further, the numerical coupling of Lagrangian particles to the carrier phase poses a challenge.

2.2.2. Forces on a particle

In the frame of the research presented in the following chapters, the specific external forces acting on a particle are given by

$$\sum \boldsymbol{f} = \boldsymbol{f}_\mathrm{g} + \boldsymbol{f}_\mathrm{coll} + \boldsymbol{f}_\mathrm{fl} + \boldsymbol{f}_\mathrm{el}\,, \tag{2.9}$$

where $\boldsymbol{f}_\mathrm{g}$ denotes the gravitational, $\boldsymbol{f}_\mathrm{coll}$ the collisional, $\boldsymbol{f}_\mathrm{fl}$ the fluid drag, and $\boldsymbol{f}_\mathrm{el}$ the electric field force acting on the particle.

The specific force due to the net effect of gravity on the particle reads

$$\boldsymbol{f}_\mathrm{g} = \left(1 - \frac{\rho}{\rho_\mathrm{p}}\right)\boldsymbol{g}\,, \tag{2.10}$$

https://doi.org/10.7795/110.20221208

where ρ_p is the particle's material density and $\boldsymbol{g}$ the gravitational acceleration. The specific collisional force term $\boldsymbol{f}_\mathrm{coll}$ accounts for both inter-particle and particle-wall collisions. Further, the specific aerodynamic drag acting on a particle is computed by the following expression, [30],

$$\boldsymbol{f}_\mathrm{fl} \;=\; -\frac{3\rho}{8\rho_\mathrm{p} r_\mathrm{p}} C_\mathrm{d} |\boldsymbol{u}_\mathrm{rel}| \, \boldsymbol{u}_\mathrm{rel} \,, \tag{2.11}$$

where C_d is the particle drag coefficient and $\boldsymbol{u}_\mathrm{rel}$ the particle velocity relative to the fluid, $\boldsymbol{u}_\mathrm{rel} = \boldsymbol{u}_\mathrm{p} - \boldsymbol{u}$. The drag coefficient is computed as a function of the particle Reynolds number, $Re_\mathrm{p} = 2|\boldsymbol{u}_\mathrm{rel}|\, r_\mathrm{p}/\nu$, according to the relation provided by Schiller and Naumann [31],

$$C_\mathrm{d} = \begin{cases} \dfrac{4}{Re_\mathrm{p}}\left(6 + Re_\mathrm{p}^{2/3}\right) & \text{for } Re_\mathrm{p} \leq 1000 \\[2ex] 0.424 & \text{for } Re_\mathrm{p} > 1000\,. \end{cases}$$

It is noted that there are other aerodynamic forces (besides drag) acting on a particle, which are neglected in the current work, summed up by the Basset-Boussinesq-Oseen (BBO) equation [32]. These include the *virtual mass force* that is required to drag along the surrounding fluid when the particle is accelerated. The virtual mass force is important for the case of a low solid-fluid density ratio which is not typical for pneumatic transport operations in process industries. The effect of a non-uniform flow around a particle is accounted for by the *Faxen force*. Further, the *Saffman force* is caused by the rotation of a particle due to large velocity gradients in shear flows. Both Faxen and Saffman forces, vanish if the particle size is small compared to the scale of the local flow gradients. The assumption of non-rotating particles also allows to neglect the *Magnus force*. The time delay in building up a boundary layer in the vicinity of the particles' surface is described by the *Basset history* term.

As can be seen, the coupling between the fluid and particulate phase is realized through the terms $\boldsymbol{F}_\mathrm{s}$ in equation (2.1b) and $\boldsymbol{f}_\mathrm{fl}$ in equation (2.11) which are related by

$$\boldsymbol{F}_\mathrm{s} \;=\; \frac{\rho_\mathrm{p}}{\rho}\,\omega \sum_{i=1}^{N} \boldsymbol{f}_{\mathrm{fl},i}\,. \tag{2.12}$$

In the above equation, N is the number of particles in a control volume in which the local particle volume fraction is given by ω.

Finally, the force acting on a particle by the electric field is given by

$$\boldsymbol{f}_\mathrm{el} = \frac{Q\boldsymbol{E}}{m_\mathrm{p}}\,, \tag{2.13}$$

where $\boldsymbol{E}$ is the local electric field strength and m_p is the mass of the particle.

2.3. Electric field

The evaluation of $\boldsymbol{E}$ requires the solution of Maxwell's equations which are presented for the sake of completeness as follows

$$\nabla \cdot \boldsymbol{E} = \frac{\rho_\mathrm{el}}{\varepsilon_0}\,, \tag{2.14a}$$

$$\nabla \cdot \boldsymbol{B} = 0\,, \tag{2.14b}$$

https://doi.org/10.7795/110.20221208

$$\nabla \times \boldsymbol{E} = \frac{\partial \boldsymbol{B}}{\partial t}, \tag{2.14c}$$

$$\nabla \cdot \boldsymbol{B} = \mu_0 \left(\boldsymbol{J} + \varepsilon_0 \frac{\partial \boldsymbol{E}}{\partial t} \right). \tag{2.14d}$$

In the above equations ρ_{el} denotes the electric charge density, $\varepsilon_0 = 8.854 \times 10^{-12}$ F/m the electrical permittivity of free space, $\boldsymbol{B}$ the magnetic field strength, $\mu_0 = 4\pi \times 10^{-7}$ H/m the permeability of free space and $\boldsymbol{J}$ the electric current density. In particular, equation (2.14a) is referred to as Gauss' law, equation (2.14b) as Gauss' law for magnetism, equation (2.14c) as Faraday's law and equation (2.14d) as Ampère's law with Maxwell's addition.

However, if one introduces the so-called electrostatic approximation, i.e., the assumption that the electric charges move much slower than the speed of light, the Maxwell equations reduce to Gauss' law (equation (2.14a)). This assumption is generally justified in flows where the electric charge adheres to particles that convey with a velocity comparable to the carrier fluid. The electrostatic approximation further implies $\nabla \times \boldsymbol{E} = 0$ which enables the expression of the electric field as the gradient of the electric potential ϕ,

$$\boldsymbol{E} = -\nabla \phi. \tag{2.15}$$

Accordingly, the electric potential satisfies the Poisson equation,

$$\nabla^2 \phi = -\frac{\rho_{\mathrm{el}}}{\varepsilon_0}. \tag{2.16}$$

Further, for the herein considered application the integral of the electric charge density over a control volume $\mathscr{V}$ that contains N particles is equal to the sum of the charges of the n particles,

$$\int_{\mathscr{V}} \rho_{\mathrm{el}} \, \mathrm{d}\mathscr{V} = \sum_{i=1}^{N} Q_i. \tag{2.17}$$

Integration of Gauss' law (equation (2.14a)) over a surface S yields by virtue of the divergence theorem,

$$\oint_S \boldsymbol{E} \cdot d\boldsymbol{S} = \frac{q}{\varepsilon_0}. \tag{2.18}$$

In the above equation, S is a surface enclosing any volume and q is the charge located within this volume. In the case of describing the electric field around a charged particle, q becomes the charge carried by the particle, Q. Further, using the spherical symmetry of the electric field surrounding a uniformly charged, spherical particle, allows solving the integrand. Assuming S to be a spherical surface yields

$$4\pi |\boldsymbol{r}|^2 \frac{\boldsymbol{r}}{|\boldsymbol{r}|} \cdot \boldsymbol{E}(\boldsymbol{r}) = \frac{Q}{\varepsilon_0}, \tag{2.19}$$

where $\boldsymbol{r}$ is a vector pointing from the particle center to any point on S. By rearranging the terms of this equation Coulomb's law is obtained, namely

$$\boldsymbol{E}(\boldsymbol{r}) = \frac{Q\boldsymbol{r}}{4\pi \varepsilon_0 |\boldsymbol{r}|^3}. \tag{2.20}$$

Thus, for the case of charged particles Gauss' and Coulomb's laws are equivalent.

3. Powder production

3.1. Introduction

Spray drying is a widely used technique in industry to produce powder by drying a multi-component liquid with a hot gas. The range of powders fabricated in this manner includes milk powder, coffee, medical ingredients, paint pigments, ceramic materials, and many more. To optimize the usability of the product, control of the resulting particle properties such as geometrical and chemical structure, bulk density, porosity, or particle size distributions is highly desirable,

An exemplary spray dryer design is sketched in figure 3.1. Usually, the liquid is injected into the device through some type of a nozzle aiming to atomize the continuous phase into a spray consisting of dispersed droplets. Whereas the outcome of atomization is of utmost importance for the characteristics of the final product, the involved processes leading to a certain droplet size distribution are manifold and highly complex (for a detailed discussion the reader is referred to Ref. [33]). In the device depicted in figure 3.1 the bulk flow direction of the hot drying gas is opposite to the injected liquid which is termed counter-current mode. While the droplets fall downwards the solvent successively evaporates until at some point the remaining solute forms a solid particle. Thus, the spray drying process consists of several strongly coupled sub-processes. Some of them, e.g. droplet evaporation, may be well understood while others, in particular the formation of particles, are due to their complexity a topic of active research.

As regards the experimental study of the drying of single droplets, acoustic levitators [34] are widely used. Albeit its obvious advantage of contact-free positioning of small samples, this technique has some flaws. For example, the inhomogeneous acoustic pressure field causes an oblate droplet shape and induces a surrounding flow [35]. The latter enhances convective mass transfer in the boundary layer [36, 37] and generates vortices inside the droplet [38], which both directly influences the liquid evaporation rate. These disadvantages motivate numerical studies.

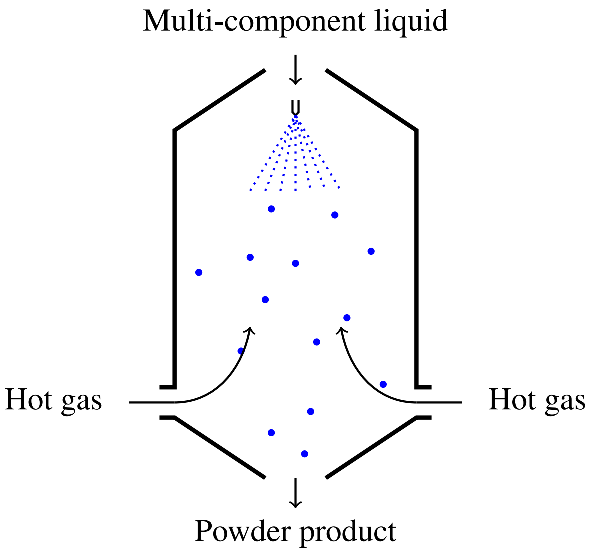

Figure 3.1.: Schematics of a counter-current spray dryer after Crowe et al. [30].

https://doi.org/10.7795/110.20221208

From a historical perspective, an important contribution represents the modeling of the evaporation of single component droplets by Abramzon and Sirignano [39] who considered the convective effect on the film thickness. As regards the drying of bi-component droplets, Nešić [40] proposed a theoretical description sub-dividing the complete process in five stages. This concept served subsequently as a base for a range of numerical models [41–44]. The existence of these stages was confirmed in several experiments (e.g. by Walton [45], Vicente et al. [46]). However, especially the last stages of particle expansion and cracking in the case of the drying temperature being above the boiling temperature was so far not taken into account in modeling approaches, neither in the references given above nor in the literature discussed in the review by Mezhericher et al. [47].

Furthermore, in addition to processes related to individual droplets, also liquid atomization and the interaction of spray particles has a strong influence on the final product properties. As regards numerical modeling of dilute spray flows, the description of the liquid phase in a Lagrangian framework and its coupling to the Navier-Stokes equations in an Eulerian framework is well established [48]. However, in case of the presence of a large number of droplets, the modeling of the spray as a continuous phase becomes an attractive approach (cf. section 2.2.1). Nonetheless, in the Eulerian framework, the discretization of a strongly polydisperse droplet size distribution is an inherent problem. This issue was addressed by the development of moment-based methods [49, 50]. One variant of moment-based methods is the direct quadrature method of moments (DQMOM) [51] which turned out to be an accurate and efficient approach to compute sprays [52]. However, even though simplified evaporation models have already been implemented, major elements of the spray drying process are still lacking in the current formulation.

In order to advance knowledge, the author studied numerically the elementary process of drying a single bi-component droplet as well as the whole spray drying process. The aim of the below-presented research was to develop a mathematical model to simulate the evaporation and drying of single bi-component droplets and the following particle formation. This model was utilized to gain an understanding concerning the influence of the drying conditions on the drying kinetics of mannitol/water droplets and the final particles. Furthermore, it was the aim to advance DQMOM to facilitate the computation of the complete spray drying process.

The following section summarizes the author's publications regarding the drying of single mannitol-water droplets [1] and the modeling of drying above the liquid boiling temperature [2]. In section 3.3 the discussion is complemented by the presentation of the author's effort regarding the computation of the complete spray drying process [3, 4].

The numerical results presented in this chapter were obtained in close collaboration with Prof. Dr. E. Gutheil (Heidelberg University).

3.2. Single droplet drying and particle formation [1, 2]

3.2.1. Mathematical model

The herein presented mathematical model is based on the characterization of Dolinski and Ivanicki [53] and Nešić and Vodnik [54] of the drying of bi-component droplets by five stages, see figure 3.2. According to their description, during stage I the droplet temperature increases to an equilibrium temperature close to the wet-bulb temperature of the surrounding gas. In the following stage II, the solvent evaporates at quasi-equilibrium conditions, i.e., heat transfer from the gas to the droplet equals the latent heat of evaporation. During this stage, the droplet shrinks while its solute mass fraction increases. The beginning of stage III coincides with the formation of a solid layer at the droplet surface. This layer diminishes heat and mass transfer abruptly giving a quick rise to the droplet temperature.

https://doi.org/10.7795/110.20221208

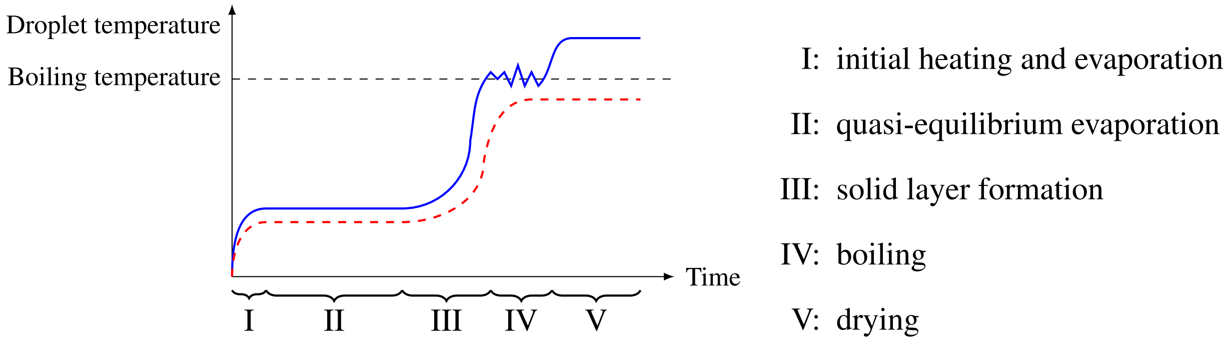

Figure 3.2.: Temperature evolution of a droplet/particle during drying below (red) and above (blue) the boiling temperature (adapted from Refs. [53, 54], reprinted with permission from Ref. [2]).

Afterward, either drying proceeds until all liquid is evaporated or, if the temperature of the drying gas exceeds the boiling temperature of the involved liquid, also stages IV and V may occur. At the beginning of stage IV, the remaining liquid inside the particle reaches its boiling point whereby the generated vapor effectuates a pressure on the solid layer. This pressure may be sufficient to inflate the particle or even exceed the solid layer strength leading to cracks or a type of explosion. If a crack appears the vapor volatilizes to the surrounding atmosphere. Consequently, the internal pressure and temperature decreases and the crack may close again which, in turn, leads to internal pressure and temperature increase. The repetition of the crack opening and closing process is responsible for the oscillations sketched in figure 3.2. Finally, when the complete liquid has evaporated the temperature of the particle rises asymptotically to the temperature of the surrounding gas during stage V.

The author developed a numerical model to predict all five stages of drying. This so-called *5-stage model* is based upon the *3-stage model* by Gopireddy and Gutheil [55] which describes the drying of bi-component droplets below boiling temperature. Both models share, assuming spherical symmetry, the one-dimensional equation for species mass conservation, namely [55]

$$\frac{\partial Y_i}{\partial t} = \frac{D_{12}}{r^2}\left[\frac{\partial}{\partial r}\left(r^2 \frac{\partial Y_i}{\partial r}\right)\right], \tag{3.1}$$

where D_{12} is the binary diffusion coefficient in the liquid and r the radial physical coordinate. The mass fraction is denoted by Y_i and the subscript $i = 1$ denotes the solvent and $i = 2$ the solute. Initially ($t = 0$), the solute and solvent are assumed to be mixed homogeneously. Due to symmetry, the zero-gradient boundary condition is imposed on Y_i at the droplet center, $r = 0$. As regards the boundary condition at the droplet surface, s, $r = r_\mathrm{d}(t)$ is given by [55]

$$-D_{12}\frac{\partial Y_i}{\partial r} - Y_i \frac{\partial r_\mathrm{d}}{\partial t} = \delta_i \frac{\dot{m}}{A\rho_\mathrm{l}}. \tag{3.2}$$

In the above equation, $\dot{m}$ is the mass evaporation rate of the respective species, ρ_l is the liquid density and A is the droplet surface area. Further, the Kronecker symbol, δ_{1i} is unity for the (evaporating) solvent and zero for the (non-evaporating) solute. The mass evaporation rate in equation (3.2) yields [39, 55]

$$\dot{m} = \frac{\sum_{i=1}^{N} 2\pi r_{\mathrm{d},i}\rho_{i,\mathrm{f}} D_{i,\mathrm{f}} \widetilde{\mathrm{Sh}} \ln(1 + B_{\mathrm{M},i})}{1 + \widetilde{\mathrm{Sh}} D_\mathrm{f} \beta / (2D_\mathrm{s}(r_\mathrm{d} - \beta))}. \tag{3.3}$$

https://doi.org/10.7795/110.20221208

Therein, the modified Sherwood number, $\widetilde{\mathrm{Sh}}$, accounts for the effect of convective droplet evaporation [39]. The vapor diffusivity and density of each component in the film are denoted by $D_{i,\mathrm{f}}$ and $\rho_{i,\mathrm{f}}$, respectively, and the diffusivity of the vapor in the solid layer is D_s. Further, $r_{\mathrm{d},i}$ is the volume equivalent partial radius of each component, $B_{\mathrm{M},i}$ is the Spalding mass transfer number [39]. Finally, if a solid layer forms at the droplet surface, its thickness β acts as a hindrance to mass transfer in the above equation.

The mathematical framework given by equations (3.1)-(3.3) was extended by Grosshans et al. [2] to account for the drying stages IV and V. In this extension, β is also considered to be zero if a solid layer exists but a crack occurs and remains zero until the crack closes again.

The energy conservation equation in the extended approach assuming a homogeneous temperature distribution, T_d, inside the droplet yields

$$m c_{p,\mathrm{l}} \frac{dT_\mathrm{d}}{dt} = \frac{\dot{m} c_{p,\mathrm{f}} (T - T_\mathrm{s})/B_\mathrm{T}}{1 + \widetilde{\mathrm{Nu}}\, k_{\mathrm{g,f}} \beta / (2 k_\mathrm{s} (r_\mathrm{d} - \beta))} - \dot{m} h_\mathrm{l} + m_\mathrm{v} c_{p,\mathrm{v}} \frac{dT_\mathrm{v}}{dt} \,. \tag{3.4}$$

where $c_{p,\mathrm{l}}$ represents the specific heat capacity of the liquid. The first term on the RHS in the above equation is the conductive and convective heat transfer from the drying gas of the temperature T to the droplet, respectively particle, having a surface temperature of T_s. In this term, B_T is the Spalding heat transfer number [39], $\widetilde{\mathrm{Nu}}$ the modified Nusselt number [39] and k_s and $k_{\mathrm{g,f}}$ denote the thermal conductivity in the solid layer and the film, respectively. The second term on the RHS of equation (3.4) represents the heat transfer related to the phase change where h_l is the latent heat of vaporization.

In comparison to the 3-stage model of Gopireddy and Gutheil [55], an additional third term is added to the RHS of equation (3.4) in the new model by Grosshans et al. [2]. This term accounts for the change of heat of the vapor inside the solid layer during expansion related to particle inflation in stage IV. The absolute heat transfer further depends on the mass of the vapor, m_v, and its specific heat capacity, $c_{p,\mathrm{v}}$. Eventually, dT_v/dt represents the change of the temperature of the vapor inside the particle which can, for small time-spans, be approximated by an isentropic process. According to fundamental thermodynamic relations, the evaluation of this expression requires knowledge of the instantaneous expansion of the particle. The expansion is characterized by the increase of its radius, Δr_p which is given by [56]

$$\Delta r_\mathrm{p} = \frac{r_\mathrm{p} \sigma_\mathrm{t}}{E} (1 - \nu) \,. \tag{3.5}$$

Therein, E and ν denote the elastic modulus and Poisson ratio of the solid layer material. The tangential stress in the solid layer can be computed as [57]

$$\sigma_\mathrm{t} = \frac{\Delta p (r_\mathrm{p} - \beta)}{2\beta} \,. \tag{3.6}$$

This equation relies on the assumption of a hollow spherical particle of a thin hull [57]. The actual expansion is caused by the pressure difference between the vapor and the ambiance, Δp, where the vapor pressure is calculated by Raoult's and Dalton's laws [55].

The derivation of the solid layer stress in equation (3.6) also allows the definition of a criteria to predict the opening of a crack by comparing its value with e.g. the ultimate tensile stress of the respective material.

For further details concerning the mathematical model, the numerical solution procedure and the utilized values of the material properties, the reader is referred to Refs. [1, 2].

https://doi.org/10.7795/110.20221208

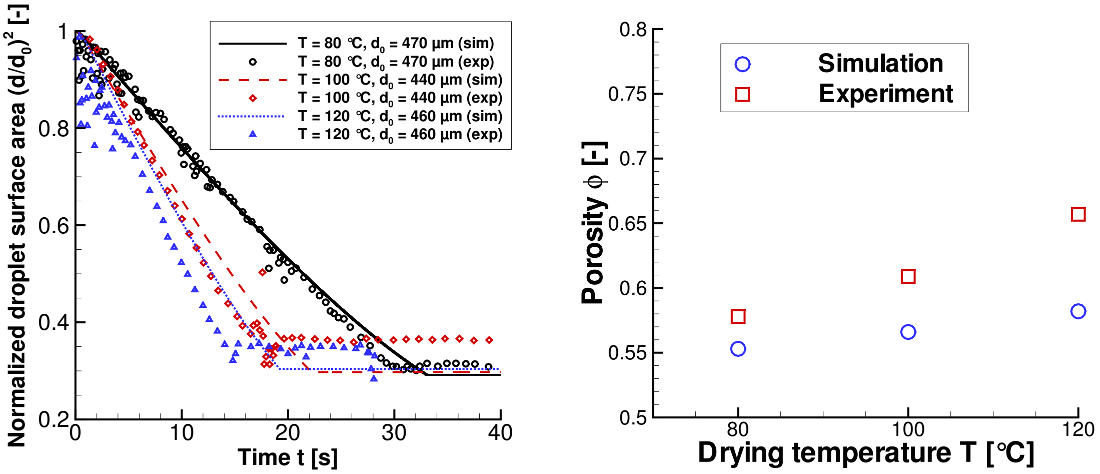

(a) (b)

Figure 3.3.: Mannitol-water droplet evaporation at different drying temperatures, $d_0 = 450$ μm, $Y_{\text{m0}} = 10$ %, (a) normalized droplet surface area versus time and (b) porosity of the final mannitol particles (reprinted with permission from Ref. [1]).

3.2.2. Results and discussion

The author carried out simulations using the 3- and 5-stage models of the drying of single droplets consisting of PVP-water and mannitol/water solutions. The computations aimed to investigate the influence of the drying conditions on the final particle characteristics. More precisely, the range of conditions included a drying temperature from 80 °C to 120 °C, a relative humidity from 1 % to 7.5 % and droplets which were initially of a diameter of 350 μm to 550 μm and a mannitol mass fraction of 5 % to 15 %. The data used for validation of the single droplet drying simulations were provided by the group of Prof. Dr. H.-U. Moritz (Hamburg University). The experiments were carried out using an acoustic levitator which is described in the publications of the author [1, 2] and in detail in the Ph.D. theses of Griesing [58] and Hellwig [59].

Exemplary, experimental data and simulations using the 3-stage model for three different drying gas temperatures, namely 80 °C, 100 °C, and 120 °C, are compared in figure 3.3(a). The curves depict the surface area of each droplet over time, respectively particle, non-dimensionalized by its initial surface area. The initial mannitol mass fraction for all three cases was 10 %. Typically, the curves decrease with time indicating the shrinking of the droplets during quasi-equilibrium evaporation of stage II. An elevation of the drying gas temperature leads to enhanced evaporation rate and, thus, a faster decrease of the droplet surface area and a steeper curve in figure 3.3(a). The shrinkage proceeds until the formation of a solid layer at the droplets' surface. This initiates stage III which is characterized by the horizontal parts of the curves.

In general, it can be concluded from figure 3.3(a) that the experimental and computational profiles agree well for the studied conditions. Also, the time instance of the solid layer formation is predicted satisfactorily by simulations. Especially the case of $T_{\text{g}} = 80$ °C is predicted excellent whereas for higher drying temperatures the simulations underestimate the final particle size. This may relate to a possible expansion of the droplets which is not included in the 3-stage model.

Figure 3.3(b) plots the porosity of the final particles, which is defined as the ratio of the hollow volume to the total particle volume, resulting from both experiments and simulations.

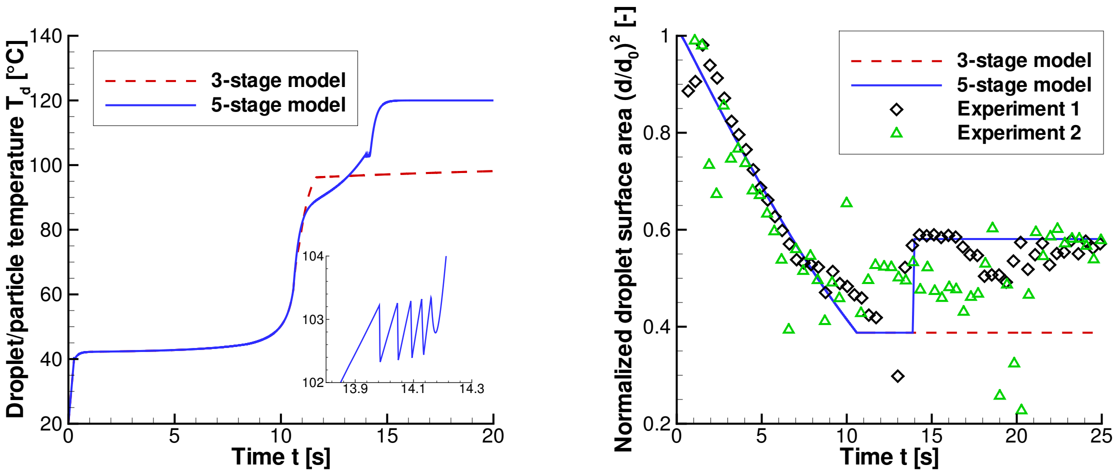

(a)

(b)

Figure 3.4.: Simulated droplet/particle temperature (a) and size in comparison with experiments (b). $T = 120$ °C, $Y_{\mathrm{m0}} = 15$ %, and $d_0 = 350$ µm (reprinted with permission from Ref. [2]).

Albeit the data agree well, the simulations give lower values whereas the highest deviation occurs for the drying temperature of 120 °C. Again, this can be explained by the expansion of the particles during stage IV which is not considered in the applied model.

Further results generated with the 3-stage model regarding the effect of the drying gas velocity, humidity and initial mannitol mass fraction are documented in publication [1].

A representative set of conditions for which particle expansion was relevant, i.e., at drying temperatures higher than the boiling temperature of the involved liquid, was computed by the author and presented in Ref. [2]. Exemplary, figure 3.4(a) depicts the temperature evolution of a droplet of an initial diameter of 350 µm and mannitol mass fraction of 15 % dried at an ambient temperature of 120 °C. The comparison of the results demonstrates that both the 3- and 5-stage model predict the first three drying stages. Nonetheless, the boiling stage, which is characterized by the oscillating temperature profile between $t = 13.9$ s and 14.2 s (see the enlargement in figure 3.4(a)) and the convergence of the particle and drying temperature at $t \approx 15.2$ s, are exclusively predicted by the 5-stage model. It is recalled, that the temperature curve stemming from the 5-stage model qualitatively replicates the theoretical prediction by Nešić and Vodnik [54] (cf. figure 3.2).

The related evolution of the droplet surface area is plotted in figure 3.4(b). Again, both models predict the surface decrease due to evaporation until the formation of the solid layer at $t = 10.6$ s. However, in opposite to the 3-stage model, the 5-stage model also predicts particle inflation due to excessive internal pressure at $t = 13.9$ s. Subsequently, the particle diameter increases fast until a crack appears and the vapor may escape. Due to inflation, the final particle size is considerably larger than predicted by the 3-stage model. The comparison of these results with two experiments conducted for the same condition reveals the substantial improvement of the 5-stage model compared to the 3-stage model in case of drying temperatures above the boiling temperature.

To further elaborate on the behavior of the new model, in figures 3.5(a) and 3.5(b) drying curves of two more droplets are given. Both droplets were also dried at $T = 120$ °C, but their initial diameter is larger than the ones considered in figure 3.4(b), namely 550 µm. Moreover, to evaluate the effect of the solute content, the initial mannitol mass fraction was decreased to

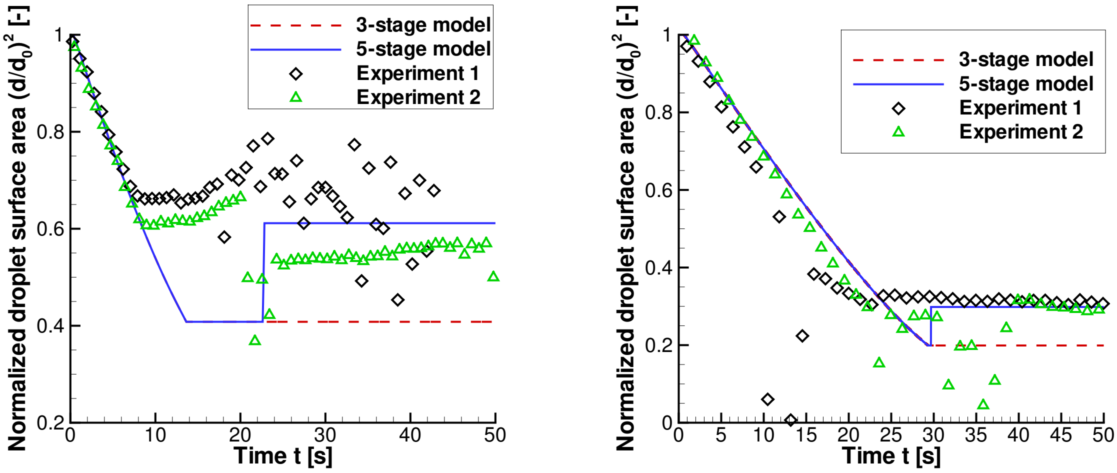

(a) $Y_{\mathrm{m0}} = 15\ \%$

(b) $Y_{\mathrm{m0}} = 5\ \%$

Figure 3.5.: Simulated droplet/particle size in comparison with experiments, $T = 120$ °C and $d_0 = 550$ µm (reprinted with permission from Ref. [2]).

5 % for the droplet analyzed in figure 3.5(b). Due to the larger diameter, the droplets contain more water which enhances the duration until solid layer formation significantly compared to the droplet of $d_0 = 550$ µm.

On the other hand, the reduction of the initial mannitol mass fraction (cf. figure 3.5(b)) results in a smaller final particle and a thin solid layer. The thin solid layer leads to an enhanced heat transfer from the surrounding gas to the particle and, thus, to a faster boiling of the liquid inside. Therefore, particle inflation initiates briefly after the solid layer formation, namely within 0.4 s compared to 9 s for cases with higher solvent content. Another consequence of the fewer amount of solvent is the establishment of a thinner and therefore less stable layer. Thus, cracks open under a relatively low internal pressure which explains the low extent of the expansion process visible in figure 3.5(b).

3.3. Spray drying [3, 4]

3.3.1. DQMOM

The numerical framework used to simulate the drying of a complete spray is based on the implementation by Gopireddy et al. [60] and was extended by the author in publication [4] as indicated in the following. In this framework, the evolution of the droplet and particle number density function during spray drying, $\zeta = \zeta(\boldsymbol{u}_{\mathrm{d}}, r_{\mathrm{d}}, T_{\mathrm{d}}; \boldsymbol{x}, t)$, is determined (cf. equation 2.5). The evolution of this quantity is analogous to Williams' spray equation [29] (compare also to equation (2.6)) given by

$$\frac{\partial \zeta}{\partial t} + \frac{\partial(\boldsymbol{u}_{\mathrm{d}}\zeta)}{\partial \boldsymbol{x}} = -\frac{\partial(\dot{r}_{\mathrm{d}}\zeta)}{\partial r_{\mathrm{d}}} - \frac{\partial(\dot{T}_{\mathrm{d}}\zeta)}{\partial T_{\mathrm{d}}} - \frac{\partial(\sum \boldsymbol{f}\zeta)}{\partial \boldsymbol{u}_{\mathrm{d}}} + \Pi_{\zeta} + \Gamma_{\zeta}\,, \tag{3.7}$$

where the extension of the author lies in the addition of the second term on RHS which accounts for the change of droplet and particle temperature during spray drying. Otherwise, $\dot{r}_{\mathrm{d}}$ is the change of the droplet radius with time and $\boldsymbol{f}$ represents the sum of specific gravitational and aerodynamic forces (cf. equations (2.10 and (2.11)). Further, Π_{ζ} denotes the droplet birth and

Γ_ζ the death rates. To compute these terms, droplet evaporation according to equations (3.3) and (3.4) and droplet coalescence by the models of Villedieu and Hylkema [61], Laurent et al. [62] are considered.

The above equation is solved using DQMOM, i.e., ζ is quadrature-based approximated as the sum over N nodes of the product of weighted Dirac-delta functions of radii, velocities [51, 60] and, according to the author's extension [4], by the temperatures, namely

$$\zeta = \sum_{n=1}^{N} w_n \delta(r_\mathrm{d} - r_{\mathrm{d},n}) \delta(\boldsymbol{u}_\mathrm{d} - \boldsymbol{u}_{\mathrm{d},n}) \delta(T_\mathrm{d} - T_{\mathrm{d},n}). \tag{3.8}$$

Introducing this approximation into equation (3.7) leads to set of transport equations for droplet weights or number densities, radii, velocities [52, 60] and temperatures [4] which reads

$$\begin{aligned}
&\frac{\partial w_n}{\partial t} + \frac{\partial (w_n \boldsymbol{u}_{\mathrm{d},n})}{\partial \boldsymbol{x}} = a_n \\
&\frac{\partial (w_n r_{\mathrm{d},n})}{\partial t} + \frac{\partial (w_n r_{\mathrm{d},n} \boldsymbol{u}_{\mathrm{d},n})}{\partial \boldsymbol{x}} = b_n \\
&\frac{\partial (w_n r_{\mathrm{d},n} \boldsymbol{u}_{\mathrm{d},n})}{\partial t} + \frac{\partial (w_n r_{\mathrm{d},n} \boldsymbol{u}_{\mathrm{d},n} \boldsymbol{u}_{\mathrm{d},n})}{\partial \boldsymbol{x}} = \boldsymbol{c}_n \\
&\frac{\partial (w_n r_{\mathrm{d},n} T_{\mathrm{d},n})}{\partial t} + \frac{\partial (w_n r_{\mathrm{d},n} T_{\mathrm{d},n} \boldsymbol{u}_{\mathrm{d},n})}{\partial \boldsymbol{x}} = d_n.
\end{aligned} \tag{3.9}$$

The terms on the RHS of these equations are determined through moment transformation of phase-space terms, which yields the linear system [60]

$$P_{k,l} = \int r_\mathrm{d}^k \boldsymbol{u}_\mathrm{d}^l T_\mathrm{d}^q \left[-\frac{\partial (\dot{r}_\mathrm{d} \zeta)}{\partial r_\mathrm{d}} - \frac{\partial \left(\dot{T}_\mathrm{d} \zeta \right)}{\partial T_\mathrm{d}} - \frac{\partial (\sum \boldsymbol{f} \zeta)}{\partial \boldsymbol{u}_\mathrm{d}} + \Pi_\zeta + \Gamma_\zeta \right] dr_\mathrm{d} d\boldsymbol{u}_\mathrm{d} dT_\mathrm{d}. \tag{3.10}$$

The exact form of the DQMOM linear system depends on the moments (k, l, q) which are chosen avoiding a singular resulting coefficient matrix.

The author coupled the DQMOM equations to the Navier-Stokes equations describing the evolution of the gaseous phase [4]. More specifically, the steady form of the DQMOM equations was solved and the turbulence in the gaseous phase was modeled by the RANS approach (cf. section 2.1.3). Thus, the time-averaged mass, momentum, energy, and species conservation equations were computed using the OpenFOAM solver *sprayFoam*. The Reynolds stresses were modeled using the standard $k-\varepsilon$ turbulence model where the turbulent kinetic energy k and its rate of dissipation ε were solved as proposed by Jones and Launder [27]. For the constants which are required to calibrate the $k-\varepsilon$ model, the standard values of Launder and Sharma [63] were used. Also, appropriate source terms were added on the RHS of the conservation equations accounting for the phase coupling.

3.3.2. Results and discussion

The author performed simulations using the above described DQMOM as well as the DQMOM coupled to RANS. Experimental validation data was provided by the group of Prof. Dr. G. Brenn (Graz University) and are given in detail by Wimmer and Brenn [64]. The experiments concerned a hollow cone spray of a PVP/water solution, where the PVP mass fraction was either 10% or 20%. The spray was injected with different pressures into a cylindrical chamber of a diameter of 1 m filled with air at atmospheric conditions. By using phase Doppler anemome-

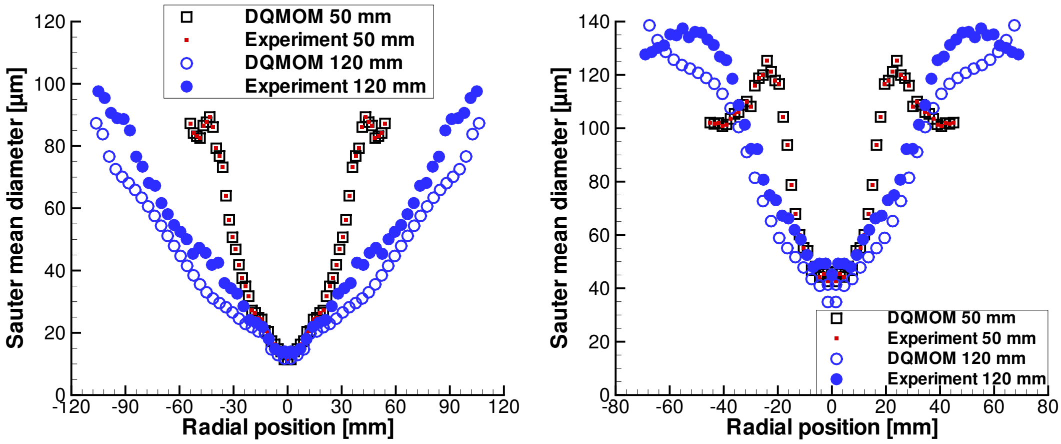

(a) Injection pressure 25 bar, 10 % PVP.

(b) Injection pressure 16 bar, 20 % PVP.

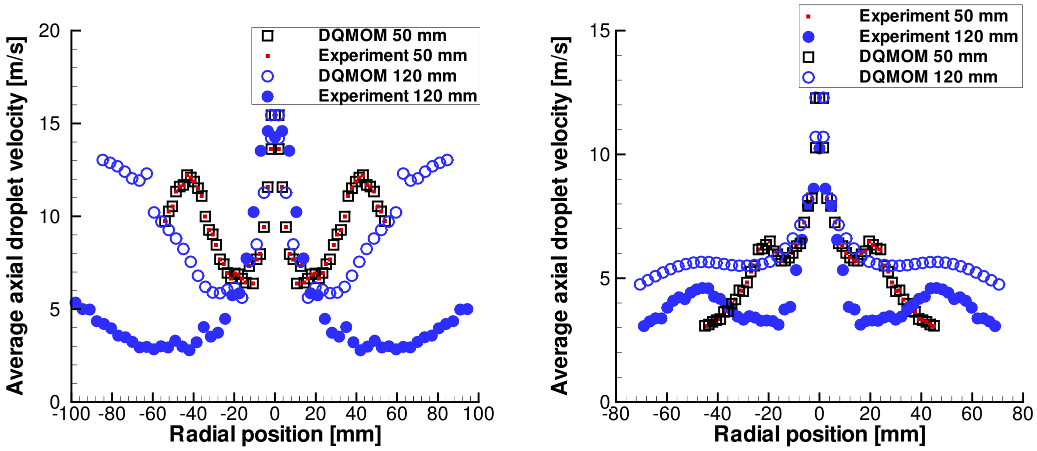

(c) Injection pressure 25 bar, 10 % PVP.

(d) Injection pressure 16 bar, 20 % PVP.

Figure 3.6.: Radial distribution of the SMD (top row) and average axial droplet velocity (bottom row) at different cross-sections. The two columns correspond to two different sprays (reprinted with permission from Ref. [4]).

try (PDA), the droplet sizes and velocities are measured at various downstream positions. Further, the data is recorded in spanwise direction at several measurement points which are separated by 1.5 mm. The experimental droplet number density is corrected using the procedure of Saffman [65] as described by Tratnig [66] and Tratnig and Brenn [67].

The same conditions as measured in the experiments were simulated by the author using DQMOM. A comparison between the experimental and numerical results of two representative conditions is provided in figure 3.6. More specifically, the figures on the left are processed from a spray consisting of 10 % PVP and injected at a pressure of 25 bar whereas the right column represents a 20 % PVP spray and an injection pressure of 16 bar. The curves in the top row depict the spanwise Sauter mean diameter (SMD) distribution whereas the bottom row gives the average axial droplet velocity. The experimental data for both SMD and droplet velocity closest to the nozzle, i.e., $z = 50$ mm, served as the basis for the generation of inlet conditionis for the simulation. The conformity of the curves at this downstream position demonstrates the suitability of the above mentioned Saffman correction procedure. The obvious widening of the

https://doi.org/10.7795/110.20221208

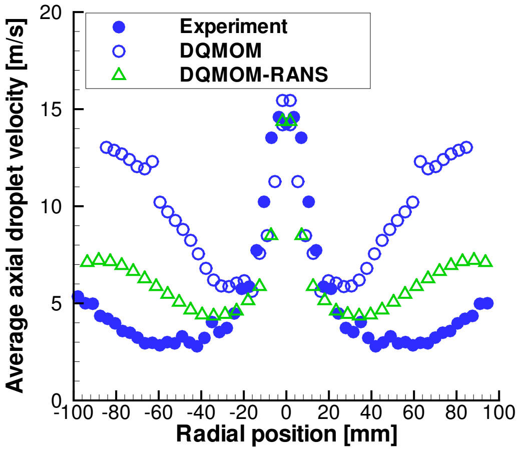

Figure 3.7.: Comparison of experimental data [64] with DQMOM [3] and DQMOM-RANS, $Y_{0,\mathrm{pvp}} = 10\ \%$, $\Delta p_{\mathrm{inj}} = 25$ bar, $z = 120$ mm (reprinted with permission from Ref. [4]).

spray at the subsequent downstream position, i.e., z = 120 mm, is a typical feature of hollow cone sprays.

Analyzing the SMD distribution in the top row of figure 3.6, one can observe that large droplets tend to migrate to the periphery of the spray whereas small droplets reside close to its centerline. This is related to airflow from the ambiance towards the spray region, i.e., air entrainment. Small droplets follow the gas flow closely due to their low inertia (cf. equation (2.7)). On the contrary, the trajectory given to large droplets at the exit of the nozzle is less disturbed by the airflow.

At the downstream position z = 120 mm, for both depicted conditions the numerical data agree in general well with the experimental results. Especially, the SMD distribution and the velocity curves in the proximity of the spray axis comply well to the measurements whereas in the periphery the results differ. The discrepancies are most pronounced for the average droplet velocity related to the higher injection pressure plotted in figure 3.6(c). This inconsistency can be explained by the missing computation of the gaseous phase when using the stand-alone DQMOM. In particular, Walzel [68] observed that the interaction with the gaseous phase causes a collapse of hollow cone sprays at a certain propagation distance. Walzel [68] argued that initially the droplets are transported along the trajectory assigned at the exit of the nozzle. Subsequently, the droplets transfer momentum to the surrounding gas which finally leads to the collapse of the hollow cone spray after which the flow behaves similarly to a free jet. This effect is not reflected in the results presented in figure 3.6.

A higher injection pressure provides more inertia to overcome surface tension and leads, thus, to the generation of smaller droplets (see the experimental correlations and theoretical discussions in Refs. [69–71]). The trajectories of small droplets are stronger influenced by the gaseous phase than large droplets due to their lower Stokes number. This explains the larger discrepancies between experiments and simulation for the high injection pressure in figure 3.6(a) and 3.6(c) compared to the low-pressure cases in figure 3.6(b) and 3.6(d). This effect is especially evident for the average axial droplet velocities which comply reasonably well for the spray injected at 16 bar but differ largely for 25 bar.

The discussion above strongly motivated the inclusion of the gaseous phase and its interaction with the liquid phase in the mathematical framework. This coupling of the phases was accomplished by the author as outlined in the previous section. The resulting axial droplet velocity profile for the most critical condition, i.e., $\Delta p_{\mathrm{inj}} = 25$ bar, is presented in figure 3.7.

https://doi.org/10.7795/110.20221208

Comparing the curve to the uncoupled simulation and the experimental data demonstrates the great improvement of accuracy of the numerical results by resolving the gas phase. Nevertheless, at the outer region of the spray,the computed axial droplet velocity differs still up to 3 m/s from the experimental measurement. This deviation may be related to inconsistent boundary conditions. To limit computational costs, the simulated domain was significantly smaller than the spray chamber. in other words, the experiments deal with a free jet whereas the simulations model a confined jet.

3.4. Conclusions

The complexity of the spray drying process stems from the large number of involved physical mechanisms taking place at a wide range of scales. In order to gain insight, the author studied numerically both the elementary process of drying a single droplet and the integral process of the complete spray evolution.

As regards the drying of a single droplet, the model predicting surface regression of mannitol/water droplets, solid layer formation, particle size, and porosity show good agreement with experimental data. The results reveal that the final particle diameter increases with increasing drying temperature, initial droplet diameter and with initial mannitol mass fraction. This constitutes valuable information contributing to the production of tailor-made particles. However, the existing model failed to predict particle drying at temperatures beyond the boiling temperature of the involved liquid which motivated the formulation of a new model by the author. This new model includes the processes of particle expansion during liquid boiling as well as the cracking and healing of the particle shell. The inclusion of the physical mechanisms in the mathematical framework greatly improves the numerical results in terms of final particle size and porosity.

Furthermore, the author employed an existing DQMOM to model the complete spray. The results regarding droplet size and velocity distribution showed a good agreement with experimental data. In order to adapt the method to the computation of spray drying, the author expanded the DQMOM to include the variations of droplet temperature. In addition, the author resolved the gas phase and coupled it to the liquid phase via momentum source terms. The coupled approach was realized by an implementation in OpenFOAM.

Within this project, several aspects of the numerical description of spray drying processes were illuminated. The main directions to be followed in future research should be the improvement of the elementary models via additional experimental data and the integration of all sub-models in one integral computational framework. As regards the latter, it is noted a full coupling of the single droplet drying model to DQMOM is still outstanding. Challenges arise especially from the connection of two models where one is formulated in a Lagrangian and the other one in an Eulerian framework. In particular, for the prediction of the onset of the solid layer in an Eulerian code, which requires detailed knowledge of the history of the individual droplet's history, to date no accurate concept is available. Nevertheless, the overcoming of these difficulties may lead in the future to a complete description of the spray drying process from atomization to particle formation.

https://doi.org/10.7795/110.20221208

4. Triboelectric particle charging [5]

4.1. Introduction

The accumulation of electrostatic charge of particles during powder handling operations originates from contact charging, also called triboelectricity. Despite its frequent occurrence in daily life, the exact nature of triboelectric charging is the topic of a long-lasting debate. There is no consensus on whether the transfer of ions, electrons, or nanoscale material patches are responsible for the effective charge transfer [72]. Furthermore, contact electrification is generally affected by numerous parameters including surface roughness [73], geometry [74], and humidity [75] which pose challenges to its theoretical description.

As regards the contact charging of particles, a significant advance in understanding the involved physics was obtained from single-particle experiments. In those experiments, a particle is accelerated under a defined impact velocity and angle towards a target. The particle charge prior to the impact is the so-called *initial charge* and the charge accumulation during impact is the *impact charge*. Through this kind of experiments, Masui and Murata [76] and Yamamoto and Scarlett [77] demonstrated that, in case of constant impact conditions, a linear relationship between both these quantities holds. This relationship is characterized by the *charging line*, see figure 4.1. Noteworthy points on the charging line are Q_0, the impact charge when the particle is initially uncharged, and the *equilibrium charge* Q_{eq}, the initial particle charge at which no further net charge transfer takes place during collisions. As revealed by Watanabe et al. [78], Q_0 increases with the impact velocity whereas Q_{eq} is independent of the impact velocity.

However, Matsuyama et al. [79] showed through their experiments that the charging line is only linear if the pre-charge is distributed uniformly on the particle surface what is generally the case for particles with a conductive surface. On the contrary, Matsuyama et al. [79] demonstrated that the measured impact charge for insulating particles exhibit a wide scattering and are hardly reproducible. Insulating particles are expected to exhibit a non-uniform pre-charge distribution since the charge spots on the surface are immobile.

The following section gives an overview of the existing literature regarding the modeling of contact charging of a particle. Partially, these formulations were implemented by the author and employed in the simulations presented in publications [6–11] which are outlined in chapter 5. Section 4.2.2 summarizes the model proposed by the author in Ref. [5] which predicts the charging of a particle while accounting for the non-uniform charge distribution on the particle's surface. Finally, the results obtained from these models are discussed and the study is concluded.

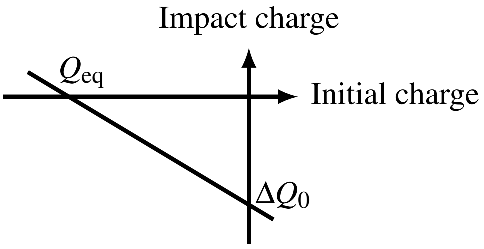

Figure 4.1.: Schematic diagram of the relationship between the impact charge and the initial charge (after Masui and Murata [76] and Yamamoto and Scarlett [77], reprinted with permission from Ref. [5]).

https://doi.org/10.7795/110.20221208

The numerical results presented in this chapter were obtained in close collaboration with Prof. Dr. M. V. Papalexandris (Université Catholique de Louvain, Belgium).

4.2. Particle charging models

4.2.1. Condenser model

A wide spread model to predict contact charging of a particle is the so-called *condenser model*. Its name refers to the analogy of the process to the temporal response of a capacitor (also known as a condenser) in a resistor-capacitor (R-C) circuit. In general, the model is restricted to conductive particles, i.e., a uniformly distributed charge distribution on the surface of the particles is assumed. Thus, herein this approach is referred to as the *uniform-charge model*. The original formulation of the condenser model by Soo [80] aimed at the computation of the charge exchange between two colliding solid spheres. According to this formulation, no charge exchange due to different contact potential takes place during collisions if both particles are of the same material. This situation is expected for particles being part of the same homogeneous powder batch. Nevertheless, charge exchange may take place if at least one of the involved particles carries a charge prior to the contact. Then, the charge transfer between two particles, $\Delta Q_n = -\Delta Q_m$, during the collision contact time, Δt_p, is given by [80]

$$\Delta Q_n = \frac{C_n C_m}{C_n + C_m}\left(\frac{Q_m}{C_m} - \frac{Q_n}{C_n}\right)\left(1 - \mathrm{e}^{-\Delta t_\mathrm{p}/\tau_\mathrm{p}}\right) = -\Delta Q_m\,. \tag{4.1}$$

In the above equation, C_n and C_m denote the capacity of both particles and τ_p their charge relaxation time.

This model was expanded by John et al. [81] to compute the impact of a spherical particle with a plane surface such as a wall or a plate. In opposite to particle-particle collisions, in this situation, the two objects in contact are usually of dissimilar material. Thus, the total impact charge from the target to the particle, ΔQ, is given by the sum of the dynamic charge transfer to the particle caused by the contact potential, ΔQ_c, and the transferred pre-charge, ΔQ_t, i.e.,

$$\Delta Q = \Delta Q_\mathrm{c} + \Delta Q_\mathrm{t}\,. \tag{4.2}$$

The dynamic charge transfer during the wall-particle contact time Δt_pw is (as for a parallel plate condenser) given by

$$\Delta Q_\mathrm{c} = -C V_\mathrm{c}\left(1 - \mathrm{e}^{-\Delta t_\mathrm{pw}/\tau_\mathrm{pw}}\right) \tag{4.3}$$

where C is the electrical capacity, V_c is the contact potential between the particle and the target, and τ_pw the charge relaxation time.

As mentioned above, it is commonly assumed [81, 82] that the pre-charge is distributed uniformly on the particles' surface. Further, if the charge within the particle-target contact area, A_pw, is completely transferred, ΔQ_t equals

$$\Delta Q_\mathrm{t} = -\frac{A_\mathrm{pw}}{4\pi r_\mathrm{p}} Q_n\,. \tag{4.4}$$

4.2.2. Model of non-uniform particle charging

The condenser model discussed in the previous section is only valid for particles of conductive surfaces. The author proposed an extension of this model accounting for the charge distribution on the surface of non-conductive particles [5]. Therefore, this new approach is referred to as the *non-uniform charge model.* In the following, the non-uniform charge model is outlined whereas the implementation and utilization of this approach in a CFD solver is part of chapter 5.

The author reformulated the condenser model for inter-particle collisions to account for non-uniform pre-charge. In the new formulation, instead of integral quantities, the local charge transfer, dq, per infinitely small surface element, s, of the particle is resolved. More precisely, during the collision of particles n and m the local charge exchanges $dq_n(s_n)$ and $dq_m(s_m)$ on the surface elements s_n and s_m, respectively, during the particle-particle contact time Δt_p are given by

$$dq_n(s_n) = \frac{C_n C_m}{C_n + C_m} \left(\frac{dq_m(s_m)}{C_m} - \frac{dq_n(s_n)}{C_n} \right) \left(1 - \mathrm{e}^{-\Delta t_\mathrm{p}/\tau_\mathrm{p}} \right) = -dq_m(s_m) \,. \tag{4.5}$$

As regards the contact between a particle and a target (e.g. a plate or a wall), the non-uniform charge model also resolves the local charge transfer, dq, at an infinite small surface element, s, of the particle as

$$dq(s) = dq_\mathrm{c}(s) + dq_\mathrm{t}(s) \,. \tag{4.6}$$

Analogous to the uniform model, in this equation dq_c and dq_t denote the dynamic charge transfer at the surface spot s and the transfer of local pre-charge, respectively. It is assumed that only the pre-charge which is located at s is transferred, i.e.,

$$dq_\mathrm{t}(s) = -q_n(s) \,. \tag{4.7}$$

Moreover, the total dynamic charge exchange is defined as the integral of its density over the particle/wall contact area, A_pw, namely

$$\int\limits_{A_\mathrm{pw}} dq_\mathrm{c}(s) = \Delta Q_\mathrm{c} \,. \tag{4.8}$$

Assuming a homogeneous dynamic charge transfer at the contact area yields

$$dq_\mathrm{c}(s) = -\frac{\Delta Q_\mathrm{c}}{A_\mathrm{pw}} \,. \tag{4.9}$$

Introducing the condenser model of equation (4.3) and the definition of the electric capacity of two parallel plates of a distance h, $C = \varepsilon_0 A_\mathrm{pw}/h$, into the equation (4.9) leads to

$$dq_\mathrm{c}(s) = \frac{\varepsilon_0 V_\mathrm{c}}{h} \left(1 - \mathrm{e}^{-\Delta t_\mathrm{pw}/\tau_\mathrm{pw}} \right) \,. \tag{4.10}$$

As regards the numerical solution of the above equations, the surface is discretized into a finite number of surface spots, n_sides, which each can carry charge. In other words, the surface element s in equations (4.5)-(4.7) and (4.10) becomes a discrete quantity. Simplifying assumptions include the random determination of the location of the contact surface on the particles' surface. Moreover, the contact area is assumed to be symmetric around its center.

The precise derivation of the variable properties in the above equations and their detailed numerical solution procedure are given in Ref. [5].

4.2.3. Alternative theoretical concepts for particle charging

As regards alternatives to the condenser model, Matsuyama and Yamamoto [83] proposed the *charge relaxation model* to predict charge separation when a particle is in contact with a solid surface. Therein, the charge transfer is calculated from the evolution of the potential difference between the particle and the wall, which increases after contact. More specifically, this model assumes discharge to be the limiting mechanism for contact charging of particles. Discharge takes place at the contact gap where the potential difference equals the gaseous breakdown limit potential, which is given by Paschen [84]. By accounting for the contribution of the initial charge through modification of the electrostatic field around the particle, Matsuyama et al. [79] were able to predict the scattering during single-particle experiments. Moreover, Matsuyama and Yamamoto [85] used the model in combination with a Monte Carlo simulation to predict the charge accumulation of a single particle during successive impacts. The non-uniform precharge was accounted for by its redistribution into an axisymmetric band charge.

Another promising theoretical formulation was established by Shen et al. [86]. They calculated the charge transfer between material surfaces from first principle physics with no empiricism or experimental input. This approach required the explicit modeling of the molecular structure of the involved materials and the electron states of the system using quantum mechanical methods. The drawback of this approach lies in its complexity and the related computational expense. Thus, their study was limited to simple systems exhibiting well-ordered structures, namely single-crystal alumina (sapphire) and silicon oxide (quartz) The expansion of this kind of investigation to relevant polymers is not feasible to date since polymers are structurally heterogeneous, often semi-crystalline, in non-equilibrium states and contain impurities.

4.3. Results and discussion

In figure 4.3 results obtained with the new non-uniform charge model are compared to data stemming from the previous uniform charge model. More precisely, the charging of a single polytetrafluoroethylene (PTFE) particle undergoing 30 successive impacts on a brass plate was computed. The particle has a radius of 50 µm and an impact velocity of 50 m/s. The detailed material properties are given in Ref. [5]. In the non-uniform model, the surface of the particle was discretized by 1000 elements.

Comparing the curves in figure 4.3 demonstrates that both models predicted the same asymptotic value. However, the time evolution of the particle charge differs greatly. In particular, both models predict the same amount of charge exchange during the first impact. This is reasonable since the particles carried initially no charge, thus, no charge distribution is present. However, for the subsequent impacts, the uniform model predicts a smooth decrease of the charge transfer. This reduction can be explained by increasing particle charge and, therefore, increasing back

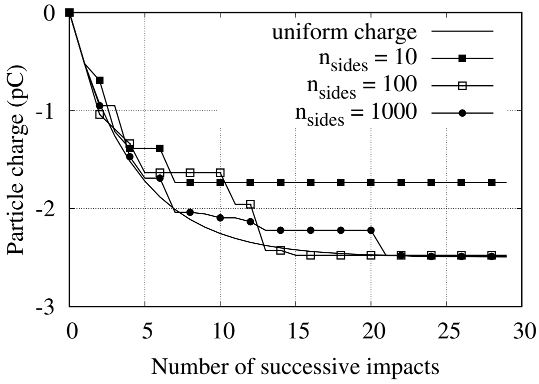

Figure 4.2.: Evolution of the charge of a single PTFE particle (r_p= 50 µm, $\boldsymbol{u}_\mathrm{p}$= 50 m/s) during successive impacts on a brass target. The non-uniform model, where the particle's surface is discretized by $n_\mathrm{sides} = 1000$ elements, predicts an equilibrium charge equal to the uniform charge model (reprinted with permission from Ref. [5]).

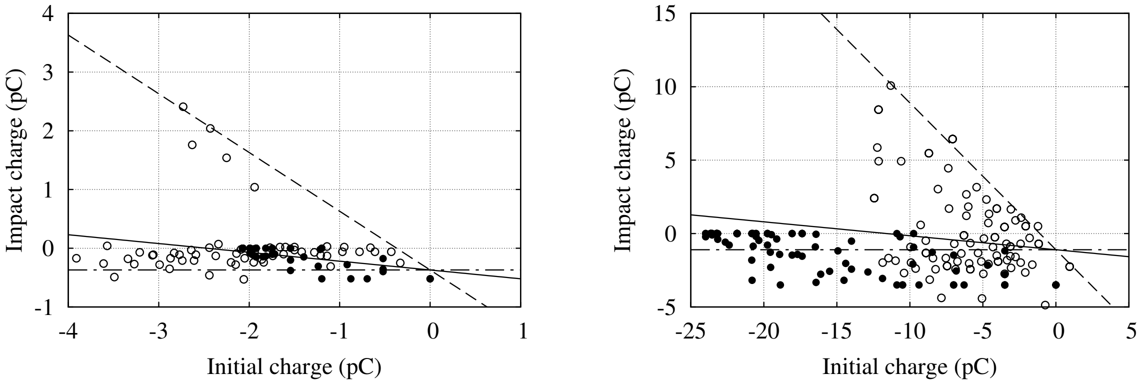

(a) $r_\mathrm{p} = 50$ µm, $\boldsymbol{u}_\mathrm{p} = 50$ m/s.

(b) $r_\mathrm{p} = 150$ µm, $\boldsymbol{u}_\mathrm{p} = 30$ m/s.

Figure 4.3.: Results of the charge relaxation model (lines) and the single-particle charging experiment (open circles) by Matsuyama et al. [79] and simulation using the non-uniform charge model (closed circles). Note that for a better visualization not all data points are shown. The solid line relates to a uniformly charged particle. The dashed line corresponds to the total charge being carried at the point of contact, while the dashed-dotted line corresponds to a charging spot remote from the contact area (reprinted with permission from Ref. [5]).

transfer of pre-charge from the particle to the target (cf. equation (4.2)). After about 25 collision events the impact charge diminishes indicating that the particle reached its equilibrium state.

On the contrary, the evolution of the particle computed by the non-uniform model is less smooth. For example, the impact charge during the third collision equals zero, while the following collision generates the same charge as the first impact. This can be explained by the influence of the location of pre-charge spots during a collision. In case the contact surface was completely covered by a pre-charge spot which was created during previous impacts no net charge is transferred (e.g., during the third collision) since dq_c and dq_t balance each other in equation (4.6). On the contrary, if the pre-charge spot and the contact area do not overlap the charge transfer is identical to the one of a previously uncharged particle (e.g., during the fourth collision). Partial overlapping of both areas leads to an intermediate amount of charge transfer in-between both described limiting cases.

Further, in figure 4.3 the results of the non-uniform charge model are compared with the experiments and calculations by Matsuyama et al. [79]. The results for two different conditions are plotted, namely figure 4.3(a) depicts the impact of particles of the size of $r_\mathrm{p} = 50$ µm with a velocity of $\boldsymbol{u}_\mathrm{p}$ 50 m/s. Furthermore, the charging of particles of $r_\mathrm{p} = 150$ µm and $\boldsymbol{u}_\mathrm{p} = 30$ m/s are plotted in figure 4.3(b). Each open circle symbol in the figures relates to a separate measurement of the impact of an individual particle carrying a variable amount of pre-charge. On the contrary, the closed circles in figure 4.3 represent in each graph the computation of the charge evolution of four particles which experience 20 successive impacts. Thus, the experimental and numerical conditions are not completely consistent. The continuous curves in figure 4.3 stem from the computations by Matsuyama et al. [79] using the charge relaxation model. Herein, the solid lines refer to uniformly pre-charged particles which correspond to the linear charging line. The other lines relate to the two limiting cases discussed above; the complete pre-charge being carried exactly at the contact area (dashed lines) and the pre-charge being located remote from the contact area (dashed-dotted lines).

As figure 4.3(a) reveals, the non-uniform charge model predicts the same equilibrium charge as the theoretical model by Matsuyama et al. [79]. Further, the scattering of the data points around the theoretical charging line lies within the bandwidth allowed by the theoretical model. The value for Q_0 is predicted slightly higher which is more pronounced for the case of the larger particle depicted in figure 4.3(b).

As regards discrepancies between the data, in figure 4.3(a) an initial charge was experimentally measured which was for some particles higher than the equilibrium charge computed by both theoretical models. This might relate to the way the pre-charge is imposed on the particles and is, thus, not reflected by the models.

Another apparent discrepancy to the computations is the significant amount of positive impact charges measured during the experiments in figure 4.3(b). These positive impact charges may again be related to the procedure of imposing the initial charge on the particle. In the simulations, on the other hand, the particle charge is accumulated by a series of identical charging events, i.e., identical contact areas and dynamic charge transfers. In this case, the pre-charge density ($q_\mathrm{t}(s)$) carried on the particle surface can not exceed the dynamic charge density acting on the contact area ($q_\mathrm{c}(s)$). Consequently, during each impact, a negative or zero charge is transferred.

Despite these discrepancies, the results computed by our new non-uniform charge model are physically sound and well supported by the experimental data.

4.4. Conclusions

The single-particle charging model is probably the main contributor to a possible modeling error in the mathematical framework presented by the author in this document. The shortcomings of the available formulations can be partially attributed to the current backlog of the research community to transfer new insights into models suitable for the implementation in CFD codes. Publication [5] by the author which was outlined in this chapter addresses this issue by proposing a model accounting for the inhomogeneous charge distribution on the particle's surface. A comparison with experimental data demonstrated that the new model computes accurately the deterministic nature of charge exchange during the collision of a particle with a target. Nonetheless, both the uniform and non-uniform charge models treat limiting cases, namely of a conductive and insulating particle surface while a general formulation is still lacking. However, the main obstacle in the development of a generally valid model to predict the charging of a single particle lies in the lack of knowledge regarding the fundamental physical charge mechanisms. Thus, further experimental work and simulations on a molecular level are essential for the advancement of current model formulations.

https://doi.org/10.7795/110.20221208

5. Charging of fluid-solid mixtures

5.1. Introduction

Particle-laden flows get electrified in a thin layer close to a solid surface where particles come in contact with a dissimilar material. Subsequently, the charge is transported away from the surface towards the bulk of the fluid-solid mixture. An amount of experimental studies, for example those by Nomura et al. [75], Masuda et al. [87], Artana et al. [88], Tanoue et al. [89], Nifuku and Katoh [90], Watano et al. [91], Watano [92], and Fath et al. [93], explored the influence of various parameters on the charging of powder, including conveying air velocity, powder mass loading, material properties of the powder, and ambient air humidity. However, their results are not conclusive because the measurements either exhibit large scatter or they do not agree with each other. These inconsistencies can be partially attributed to the feed of a powder into an experimental facility which causes an unwanted electric charging that is very challenging to control. Also, uncertainty concerning the inlet boundary conditions contributes to the scattering of experimental results.

These difficulties provided motivation for numerical studies of triboelectric charging. However, in past investigations, owing to the computational expense of full-scale simulations, the dynamics of the flow was often represented in a rather simplified manner. For example, Watano et al. [91] assumed a pre-defined velocity profile for the carrier fluid. A more realistic approach was followed by Kolniak and Kuczynski [82] and Tanoue et al. [89, 94] who simulated triboelectric charging of powders solving the RANS equations. However, RANS cannot resolve the interaction of turbulence with the particle dynamics which is crucial for the charging process. This interaction was computed through LES by Lim et al. [95] and Tanoue et al. [96]. In particular, they elucidated the influence of the electric field on particle trajectories during pneumatic conveying and in toners of electrophotography systems. Nonetheless, these two studies did not focus on the charge build-up; instead, they assumed a pre-defined and constant particle and pipe charge. Thus, detailed LES of triboelectric powder charging, including the study of the influence of the conveying conditions, was still outstanding.

Over the years DNS has become a computationally affordable tool to study particle-laden flows. For example, McLaughlin [97] discovered, using DNS, the fundamental principles of *turbophoresis*, i.e., the tendency of particles to migrate in the direction of decreasing turbulence level. However, to the best of the author's knowledge DNS of tribolectric charging were not available in the literature.

The author closed the gap of lacking LES and DNS regarding the accumulation of electrostatic charge in fluid-solid flows. The corresponding publications are outlined in the following sections. Section 5.2 elaborates on the physical mechanisms of the transport of charge within the flow which were identified in Refs. [6, 7]. In sections 5.3.1–5.3.3 the author's research concerning charge accumulation in pipe flows, discussed in Refs. [8–11], is summarized. Section 5.3.4 represents a side branch of the actual research direction, namely the prediction of the electrostatic charging of helicopters flying through a dust storm (Refs. [12, 13]).

The numerical results presented in this chapter were obtained in close collaboration with Prof. Dr. M. V. Papalexandris (Université catholique de Louvain, Belgium).

https://doi.org/10.7795/110.20221208

5.2. Charge transport mechanisms

5.2.1. Direct numerical simulations [6]

In publication [6], the author studied the triboelectric charging of particles in a turbulent channel flow. As regards the applied mathematical model, the mass and momentum balance laws (equations (2.1a) and (2.1b)) were solved for the fluid phase. All flow scales were resolved on the numerical grid, i.e., direct numerical simulations were performed. The particles were computed in a Lagrangian framework where the acceleration of a single particle is given by equations (2.8)–(2.13). Further, the electrostatic field strength is calculated through equations (2.15)–(2.17). Electric charge exchange between particles and the channel walls and in-between particles is predicted by the uniform-charge condenser model, i.e., equations (4.1)–(4.4).

The Reynolds number of the fluid flow based on the mean centerline velocity, u_c, and the half-width of the channel was 3300. Periodic boundary conditions were applied at the streamwise and spanwise directions to mimic infinite-size parallel plates. Initially, the particles are distributed randomly in a fully developed turbulent flow with velocities equal to the local fluid velocity. Further, the particles are monodisperse and of a diameter of 1/1800 times the channel half-width.

Two exemplary instantaneous flow-fields for the conditions $Ri = 0$, $St = 20$, $\omega = 0.23 \cdot 10^{-6}$, and $U = 1$ are depicted in figure 5.1. Herein, t^+ is the physical time non-dimensionalized with the friction velocity and the half-width of the channel. A Richardson number, Ri, of zero means that gravity is neglected. As regards St (cf. equation (2.7)), τ_r is derived assuming a low particle Reynolds number [30, 98] and τ_f is defined in terms of the channel half-width and the centerline velocity. Further, ω denotes the volume fraction of the particulate phase. Finally, U is the contact potential non-dimensionalized by a reference potential U_0 that is set equal to 1 V.

In figure 5.1 the particle charge is expressed in terms of the absolute non-dimensional specific charge σ which is defined as

$$\sigma = \frac{|Q|\,U_0}{m_\mathrm{p}\,u_\mathrm{c}^2}\,. \tag{5.1}$$

Figure 5.1 indicates that the particles in the vicinity of the walls carry, on average, the highest charge whereas the number of charged particles in the bulk of the flow increases with time. This

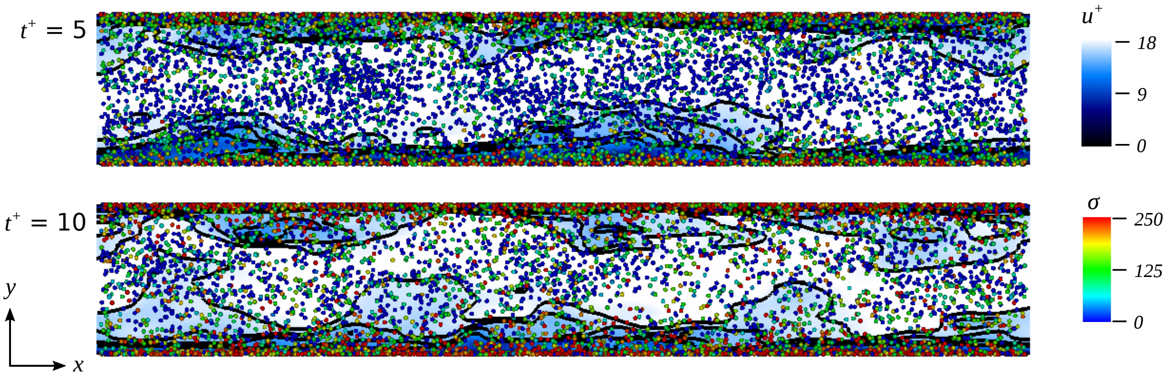

Figure 5.1.: Instantaneous visualizations of the flow patterns of the case of $Ri = 0$, $U = 1$, $St = 20$ and $\omega = 0.23 \cdot 10^{-6}$. The black contours represent the isolines of the magnitude of the fluid velocity. For visualization purposes, the particles are enlarged and only every other particle is shown. The x-axis points to the streamwise direction and the y-axis to the wall-normal direction (reprinted with permission from Ref. [6]).

https://doi.org/10.7795/110.20221208

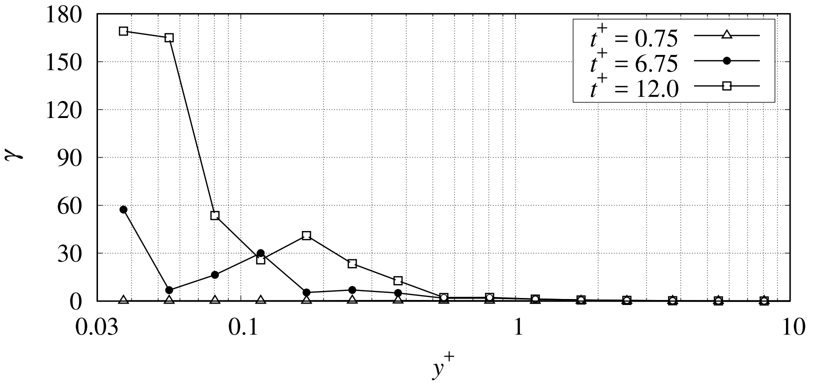

Figure 5.2.: Evolution of the profiles of the linear charge density γ for the case E ($Ri = 0$, $U = 1$, $St = 2$ and $\omega = 0.23 \cdot 10^{-6}$). The charged particles, hence the electrostatic charge, migrate away from the wall. However, this process is so slow that the electric charge remains practically confined within a thin layer very close to the wall (reprinted with permission from Ref. [6]).

implies that the particles accumulate charge during wall collisions and subsequently migrate towards the center of the channel which is referred to as *particle-bound charge transport*. Also, it can be inferred that due to *turbophoretic drift* the particles tend to adopt a location close to the walls. Thus, particle-bound charge transport and turbophoresis are counter-acting mechanisms, as regards the charging patterns and distribution of electric charge across the channel.

According to the findings of the author, an increase of the Stokes number implies that the particles are affected less by the flow structures. This results in a higher frequency of particle-wall collisions and, thus, enhances the charging rate of the particulate phase. In contrast, for the conditions presented in figure 5.1 but a low Stokes number, $St = 0.2$, the particles follow closely the flow streamlines and the amount of electric charge accumulated by the particles is negligible.

When the Stokes number was increased to 2 while keeping the other parameters constant the location of the peak value of the particles' number density is significantly shifted towards the wall. This results in a sufficiently high particle-wall collision frequency to cause significant particle electrification. The resulting profiles of the linear charge density γ, defined as charge per viscous lengthscale in the wall-normal direction, are plotted in figure 5.2. In this figure, the distance from the wall is given by $y^+ = y/\delta_\mathrm{v}$ with δ_v being the viscous lengthscale. From this plot it is inferred that the particles get charged at the wall but, due to low particle dynamics, the electric charge remains confined within a thin layer close to the wall. More specifically, throughout the duration of the simulation, most of the electric charge is still located in the viscous sublayer.

In the case of a high Stokes number, $St = 20$, the charging rate of particles is significantly increased. Here, the momentum of these particles in the wall-normal direction is sufficient to cross the viscous sublayer without getting trapped by the near-wall structures of the flow. This causes a different charge distribution for $St = 20$ as can be seen in figure 5.3. In particular, we observe that at $t^+ = 12$ the peak of γ is detached from the wall. Moreover, a significant amount of charge is transported due to their inertia towards the bulk of the channel via particle-bound transport.

The influence of the particle volume fraction is analyzed by increasing the number of particles by factor ten, i.e., $\omega = 2.3 \cdot 10^{-6}$ while St remains 2. This increase results in more inter-particle collisions per particle and time unit. This has important consequences, namely the appearance of a new charge transport mechanism which is herein referred to as *inter-particle charge dif-*

https://doi.org/10.7795/110.20221208

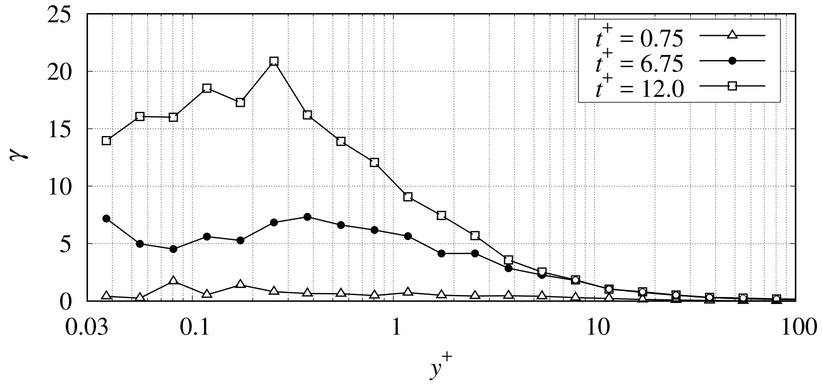

Figure 5.3.: Evolution of the profiles of the linear charge density γ for the case of $Ri = 0$, $U = 1$, $St = 20$ and $\omega = 0.23 \cdot 10^{-6}$. At high Stokes numbers, a significant amount of electric charge migrates towards the centerplane of the channel via particle-bound charge transport (reprinted with permission from Ref. [6]).

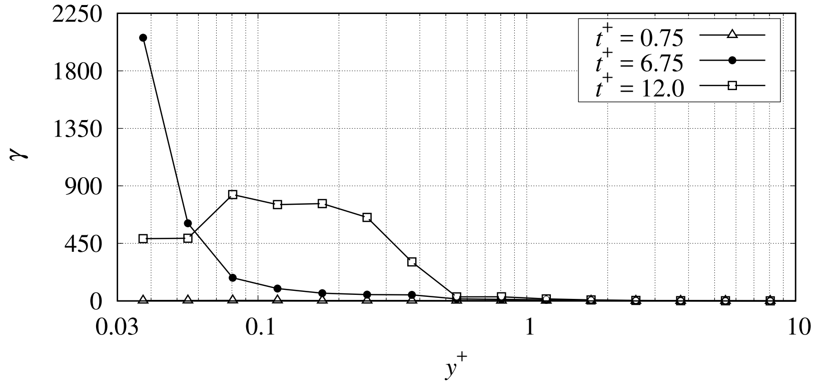

Figure 5.4.: Evolution of the profiles of the linear charge density γ for case of $Ri = 0$, $U = 1$, $St = 2$ and $\omega = 2.3 \cdot 10^{-6}$. Due to a large number of particles and inter-particle collisions, the dominant mechanism of charge transport is inter-particle charge diffusion (reprinted with permission from Ref. [6]).

fusion. More specifically, due to the increased collision frequency, the charge exchange via inter-particle collisions increases whereas the particle mean free path becomes shorter and particle-bound charge transport attenuates. The effect of this mechanism can be evidenced by the profiles of the linear charge density γ that are presented in figure 5.4. Here, in opposite to the corresponding profile for the case with fewer particles, cf. figure 5.2, charge migrates away from the channel wall through inter-particle charge diffusion. Nevertheless, most of the accumulated charge remains confined in the area $y^+ < 1$.

5.2.2. Inter-particle charge diffusion [7]

Due to its novelty, the author dedicated a subsequent study to further explore the importance of the mechanism of inter-particle charge diffusion (see the previous section) for certain flow conditions. This study was performed through an idealized numerical setting. Therein, the trajectory of each particle was computed individually in a Lagrangian framework (equation (2.8)). As regards forces on the particles, collisional and electric field forces were accounted for whereas

https://doi.org/10.7795/110.20221208

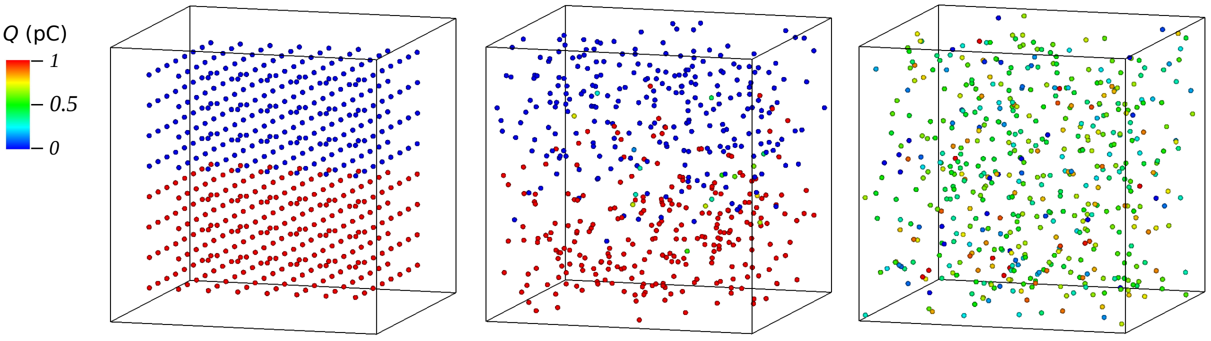

(a) $t = 0$ s

(b) $t = 0.05$ s

(c) $t = 0.5$ s

Figure 5.5.: Instantaneous snapshots of the computations of 512 particles released in a cube of the side length of 8 cm. Figure (a) shows the initial condition. After 0.05 s (b) few particles exchanged charge through collisions. Moreover, after 0.5 s (c) the charge is rather homogeneously distributed through inter-particle charge diffusion (reprinted with permission from Ref. [7]).

aerodynamic and gravitational forces were neglected. More specifically, the force due to an electric field acting on a particle was calculated by the superposition of the Coulomb forces (equation (2.20)) of the surrounding particles. Charge exchange in-between particles during collisions was predicted by the uniform condenser model (equation (4.1)).

The cubical computational domain employed in this study is visualized in figure 5.5(a). In order to focus on the interaction between particles, charge exchange during wall collisions was not taken into account. In the simulation shown in figure 5.5 512 particles of the surface resistivity $\varphi = 10^6$ Ωm, the elasticity parameter 8.4×10^{-7} m s^2/kg, $r_\mathrm{p} = 100$ µm, and $\rho_\mathrm{p} = 4000$ kg/m^3 were released, resulting in a number density of 1 cm^{-3}. In the beginning ($t = 0$ s, figure 5.5(a)) the particles were distributed equally spaced and assigned with an equal velocity amplitude. However, the direction of the velocity vector of the particles was ascribed randomly. In order to mimic a scenario similar to the real situation in a flow, the particles at the bottom half of the domain were charged whereas those at the top half were uncharged. This idealizes the situation of particles residing close to the wall and gaining charge and other particles being located in the bulk of the flow, which was discussed in section 5.2.1. In the case depicted in figure 5.5, the initial charge of the charged particles is 1 pC.

The particle positions and their charge after 0.05 s are given in figure 5.5(b). While the majority of the charge is retained at the bottom of the domain a charge mixing layer is formed in the central region. In this layer, charge was redistributed through collisions of charged and uncharged particles. Further, figure 5.5(c) shows the situation after $t = 0.5$ s. Here, the charge is apparently mixed rather homogeneously in the domain which suggests an effective inter-particle charge diffusion.

The study focused on the evaluation of the most relevant flow parameters on the efficiency of the inter-particle charge diffusion process. In order to provide a measure for the efficiency, the root mean square (rms) of the charge distributions was computed as

$$Q_\mathrm{rms} = \left(\frac{1}{N} \sum_{i=1}^{N} \left| Q_i - \overline{Q} \right|^2 \right)^{1/2} , \tag{5.2}$$

where $\overline{Q}$ denotes the average particle charge. It turned out that the time evolutions of Q_rms resemble closely an exponential decay function. This allows to derive the time scale of the

https://doi.org/10.7795/110.20221208

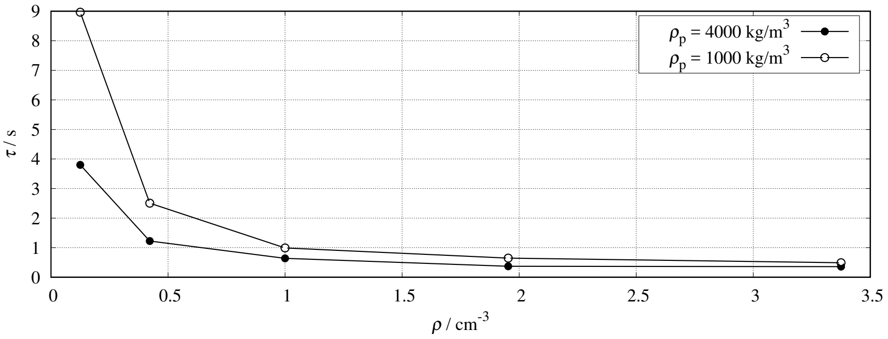

Figure 5.6.: Decay time scale versus particle number density (reprinted with permission from Ref. [7]).

decay, τ. Evidently, τ can be interpreted as a time-scale that characterizes the efficiency of inter-particle charge diffusion. The smaller it is, the more efficient the charge transferred via inter-particle collisions becomes.

Therefore, τ was used to evaluate the importance of this mechanism for different flow conditions. Exemplary, figure 5.6 depicts the influence of the particle number density on τ for two different particle material densities. An increase in ρ_p leads to a higher particle kinetic energy and, thus, more severe collisions. Severe collisions cause more charge exchange and, consequently, smaller values for τ. In addition, a higher number density leads to a higher collision frequency which also results in smaller decay times. In figure 5.6, τ seems to asymptotically approach zero, indicating that for a very high particle number density inter-particle charge diffusion occurs almost instantly. On the contrary, at low number densities, no collisions take place and, therefore, τ grows asymptotically.

An interesting region in the figure, with respect to inter-particle charge diffusion, can be identified around the data point for a number density of 3.375 cm^{-3} and a material density of $\rho_\mathrm{p} = 1000$ kg/m^3. Here, τ is low due to the high particle number density, thus, inter-particle charge diffusion is effective. At the same time, the particles' inertia is low which means that for these conditions inter-particle charge diffusion might be the dominating mechanism to transport charge in space. For the same number density but higher values of ρ_p inter-particle charge diffusion is still effective, however, here particle-bound charge transfer is expected to be more important.

5.3. Charge accumulation

5.3.1. Pipe flows [8–10]

In publications [8–10] the author studied the build-up of electrostatic charge during pneumatic conveying in pipes.

Publication [8] regarded the implementation of a suitable numerical framework which was used subsequently in the other investigations outlined within this section. In this approach, the spatially filtered mass and momentum balance laws (equations (2.1a) and (2.1b)) were solved for the fluid phase. Thus, the large-scale turbulent structures in the flow field were directly resolved on the grid by LES. In contrast, the residual (sub-filter scale) stresses are modeled by the dynamic Smagorinsky model. The Smagorinsky constant was calculated by the dynamic approach of Germano et al. [22] using the least-square technique and averaging in the streamwise direction as proposed by Lilly [99].

https://doi.org/10.7795/110.20221208

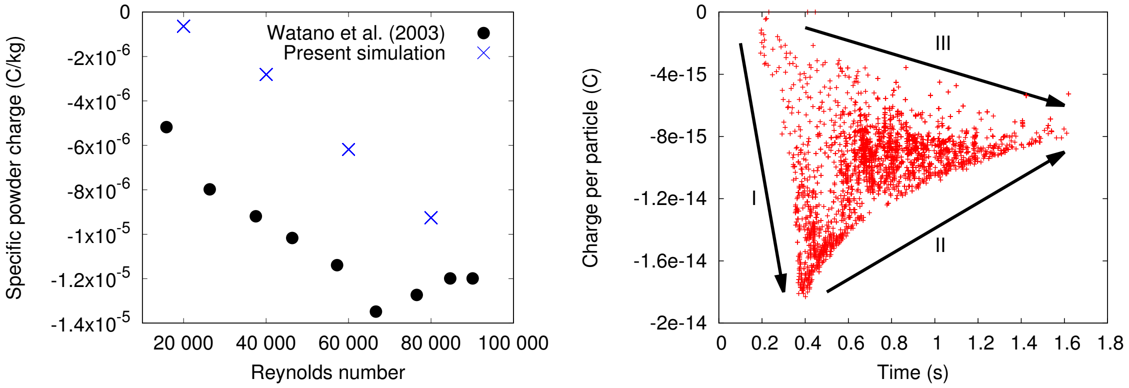

(a) (b)

Figure 5.7.: (a) Simulation of the charging of 10 g PMMA particles compared to experimental data by Watano et al. [91]. (b) Simulated particle charge when leaving the pipe for an airflow of Re = 20 000 (reprinted with permission from Ref. [8]).

The particles were treated in the same way as in the above-described DNS study (cf. section 5.2.1), i.e., in a Lagrangian framework. The acceleration of each single particle is given by equations (2.8)–(2.13). Charge exchange between particles and the pipe walls and in-between particles is predicted by the uniform-charge condenser model, i.e., equations (4.1)–(4.4).

In publication [8] the charging of a monodisperse polymethyl methacrylate (PMMA) powder in a perfectly grounded pipe was studied. The numerical set-up resembles the experimental data of Watano et al. [91], who piled 10 g of particles of a diameter of 300 µm at the beginning of a steel pipe of an inner diameter of D = 36 mm and a length of L = 2 m. The particles were transported pneumatically through the pipe and their specific charge was measured at the outlet of the pipe.

The comparison between simulations and experiments of the specific charge regarding the complete powder is shown in figure 5.7(a). In both the simulations and the experiments the specific powder charge increases approximately linearly with the conveying air velocity and the slopes of the curves match exactly. Responsible for this effect is the stronger turbulent dispersion of particles at higher air velocities leading to more frequent and stronger particle-wall collisions and, subsequently, to a higher powder charge. As regards discrepancies between experimental and numerical results, the experiments by Watano et al. [91] reveal a reduction of the specific powder charge for flow Reynolds numbers higher than 70 000. Whereas several explanations for this behavior are proposed in Ref. [8], definite proof is lacking. Therefore, $Re = 70000$ was assumed to represent the upper limit of the model validity. In addition, the experimental results show a constant offset of about -6 µC/kg to the simulation. This offset may be attributed to unwanted contact charging during the feed of the particles to the facility.

To further analyze the numerical data, the charge of each particle at the time instance when leaving the pipe is visualized for $Re = 20000$ in figure 5.7(b). The cloud of data points allows distinguishing two stages of powder output. The first stage, which is indicated by arrow I in figure 5.7(b), lasts up to about t = 0.4 s. During this stage, the average charge of the particles leaving the pipe increases with time until a maximum value of $-1.8 \cdot 10^{-14}$ c is reached. The low charge in the beginning corresponds to the first particles that move through the pipe with only a few collisions with the pipe wall or with other particles. Later particles, when the flow is more dense, are slowed down when colliding with other particles. These slower particles have a longer residence time in the pipe, collide more frequently with the pipe wall, and obtain, therefore, a higher charge. During the second stage the spanwidth of the particle charge distri-

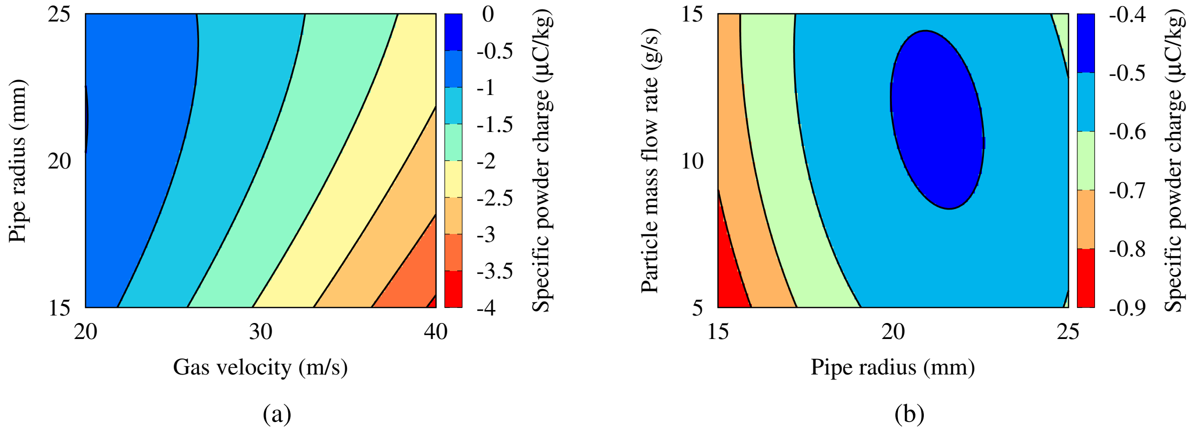

(a)

(b)

Figure 5.8.: Contour plots of the specific powder charge, for (a) a constant solid mass flow rate of 10 g/s and (b) a constant gas velocity of 20 m/s (reprinted with permission from Ref. [9]).

bution becomes more narrow. More specifically, the charge of the low-charged particles further increases as indicated by arrow III whereas the charge of the highly charged particles decreases (follow arrow II). This can be explained by the charge transfer during inter-particle collisions becoming dominant in this stage, which confirms the findings presented in section 5.2.2.

The implemented numerical framework was subsequently employed in publication [9] to investigate the influence of design parameters of the pneumatic piping system on powder charging. To this end, average gas velocities from 20 m/s to 40 m/s, solid mass flow rates from 5 g/s to 15 g/s, and pipe radii between 15 mm and 25 mm were considered. In order to reduce the number of required simulations and to analyze the results, a Design of Experiments (DoE) methodology was applied. DoE offers the possibility to reveal the relation between influential factors and responses, i.e., depending variables. More specifically, a 3-level face-centered central composite design (CCF) plan was chosen.

The final analysis showed that the gaseous flow rate is an important parameter in the entire range studied herein, whereas the pipe radius has only a strong effect for small pipes. The influence of both parameters on the powder charge is depicted in figure 5.8(a) for the case of a solid mass flow rate of 10 g/s. Further examination of the data demonstrated that in a smaller radius the particles are frequently reflected from one pipe wall to the other, thus, accumulating a high charge. In contrast, for the larger pipe, the particles travel a longer distance until they experience the next collision with the wall.

An interesting behavior is observable in figure 5.8(b) which depicts the case of a conveying air velocity of 20 m/s. For these conditions, a sweet spot representing a low powder charge is present for a particle mass flow rate of 12 g/s and a pipe radius of 33 mm. This sweet-spot is equivalent to the region of low charge in figure 5.8(a). In terms of plant safety, this can be considered as an optimized conveying condition.

Finally, in publication [9] the author evaluated the influence of the material properties of the powder and pipe on electrostatic charging. The simulations revealed that the particles Poisson ratio and Young modulus, its electrical resistivity, as well as the permittivity represent promising measures to control the charge of the powder. More specifically, an increase of each in these quantities by 50% may lead to a decrease in the powder charge of up to 40%.

https://doi.org/10.7795/110.20221208

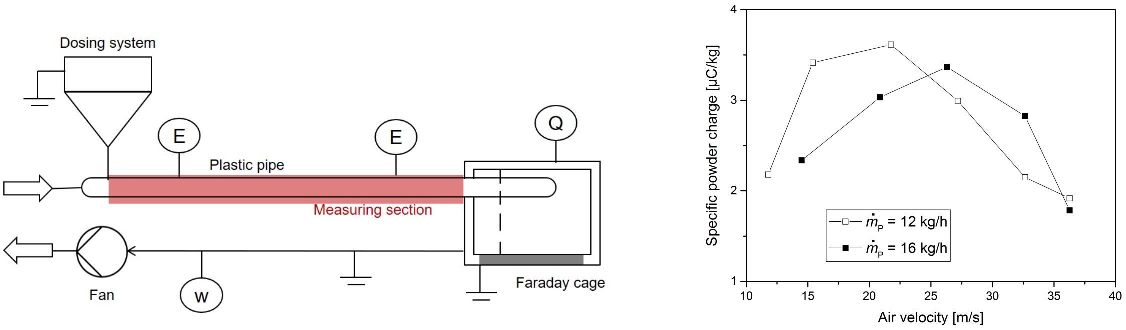

(a) (b)

Figure 5.9.: (a) Design of the experimental rig where W, E, and Q are the measurement devices for the air velocity, electric field strength, and powder charge, respectively. (b) Measured specific charge of PMMA powder transported in a PTFE pipe of an inner diameter of 30 mm, depending on the air velocity and the solid mass flow rate ($\dot{m}_\mathrm{p}$) (reprinted with permission from Ref. [11]).

5.3.2. Experimental investigations [11]

For the development of numerical models as well as for their validation the availability of reliable experimental data is crucial. Due to its high sensitivity to initial and boundary conditions, the process of charge build-up is challenging to study experimentally, and reliable validation data for numerical models is scarce. Therefore, an experimental facility to measure the charging of powder during pneumatic transport was set up in the group of the author at PTB, Braunschweig. The set up of the facility and all tests reported in publication [11] were realized within the MSc project of N. Schwindt under the guidance of Dr. D. Markus, Dr. U von Pidoll, Prof. Dr. U. Klausmeyer (all PTB, Braunschweig) and the author.

The investigations regarded the influence of a range of parameters on the triboelectric charging of powders and transport pipes. Due to its placement in a climatic chamber, the test-rig facilitates the control of the ambient conditions to a high degree. The test-rig can be operated in discontinuous or continuous (see figure. 5.9(a)) mode, while the latter allows for the analysis of a significantly larger amount of powder. The measurements confirmed the previous observation that the powder charge first increases with an increase in conveying air velocity until it reaches a maximum beyond which it subsequently drops (see figure 5.9(b)).

It was found that the air velocity that maximized the powder charge depends on the pipe material, diameter, and powder loading. Further, a larger pipe diameter proved to enhance the charging process significantly. Moreover, we observed that the transferred charge changes its sign depending on the mode of operation of the test-rig. It was anticipated that the increased number of particle-pipe collisions in continuous mode would modify the local properties of the contact surface, thereby altering the charging process. Due to the careful control of the ambient conditions, the results were highly repeatable, demonstrating the capability of the test-rig to generate data for model validation. However, the reasons underlying the charge drop beyond a certain air velocity and the change of the sign of the charge remained within this study an open question.

5.3.3. Non-uniform particle charging [5]

To investigate the charging of particles with non-conducting surfaces, the author implemented the non-uniform charge model (cf. section 4.2.2) into the CFD solver. In particular, the transport of a powder consisting of monodisperse PTFE particles of a size of r_p= 150 µm through a pipe

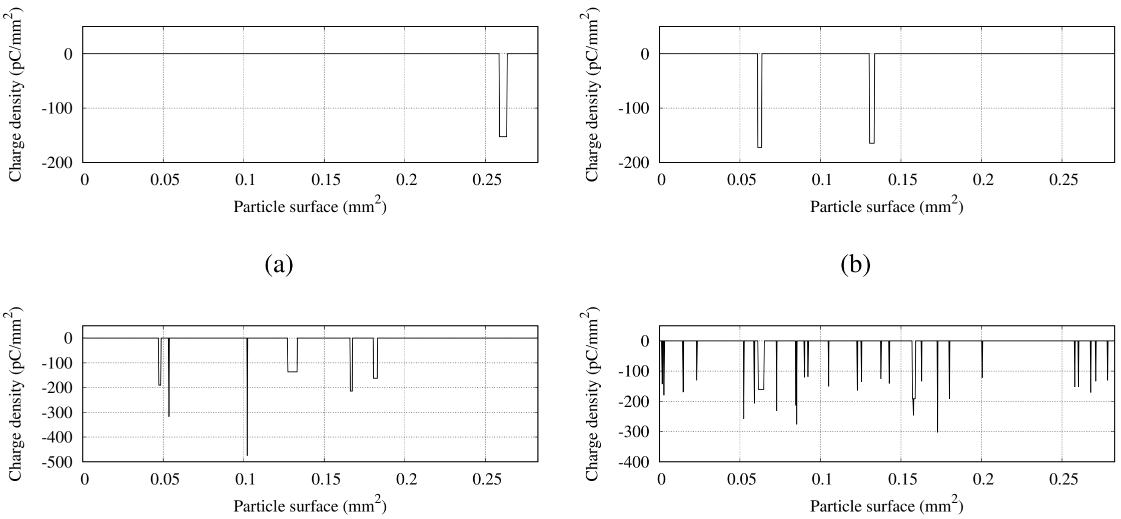

(a) (b)

(c) (d)

Figure 5.10.: Profile of the charge density on the surface of four particles representing different stages of conveying (reprinted with permission from Ref. [5]).

of a length of 2 m and a diameter on 40 mm was studied. The Reynolds number of the gas was 82 000 and the solid mass loading 20 g/s.

The state of four particles each representing a different stage of the conveying process is further analyzed in figure 5.10. Particle 1, whose charge density profile is displayed in figure 5.10(a) is at an early stage, i.e., short after injection in the pipe. Thus, it experienced so far only one collision with the wall, leaving one charging spot around the particle surface location 0.26 mm^2 and carrying a charge density of -150 pC/mm^2. Particle 2 propagated further and its charge density profile (figure 5.10(b)) reveals that it experienced a second wall contact which imposed a second charge spot at the surface. The third particle (figure 5.10(c)) is about to reach the end of the pipe. Thus, it experienced several contacts with the wall which each left a spot of different size and charge density on its surface. However, since the spots are of relatively small size compared to the particle surface, each charging process did not interact with the pre-charge.

Particle 4 (figure 5.10(d)) is also close to the end of the pipe but interacted, due to its specific trajectory, more frequently with the wall than particle 3. Therefore, its dynamic charging acted several times on surface areas that already carried pre-charges. For instance, figure 5.10(d)) reveals a double charged spot around the particle surface position 0.16 mm^2. Here, a large spot carrying -190 pC/mm^2 can be identified which is superimposed by a small spot of -245 pC/mm^2.

In order to get a deeper insight in the behavior of the respective charging model, impact vs. initial charge diagrams for inter-particle collisions are plotted in figure 5.11. The plots show the results of two simulations of identical conveying conditions. However figure 5.11 relates to particles with a conductive surface, i.e., the uniform charging model was used, whereas figure 5.11 depicts the case of non-conductive particles, i.e., the non-uniform charging model was applied. Note that here the initial charge refers to the total charge difference between both particles prior to their impact.

Obviously, the uniform and non-uniform charge models predict a qualitatively and quantitatively different charging process. One fundamental difference between both is that the uniform charge model always predicts a charge transfer in case the particles carry different initial charges. The data points are symmetric to the origin of the graph, i.e., which of the particles

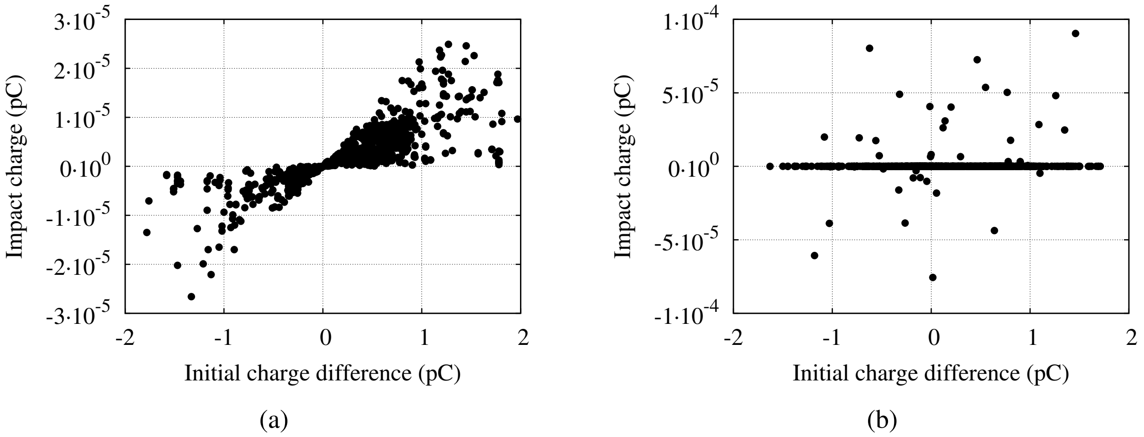

Figure 5.11.: Impact vs. initial charge diagrams for inter-particle collisions computed with the (a) uniform charge model and (b) the non-uniform charge model. Note that here the initial charge relates to the initial charge difference between both particles (reprinted with permission from Ref. [5]).

carries the higher initial charge affects only the direction of the charge transfer but not its absolute value. The impact charge scatters between a maximum and minimum value depending on the inter-particle contact time and area.

On the contrary, the non-uniform charge model predicts for most collisions a zero charge transfer even if the charge of both particles prior to contact is different. This can be explained by the high probability that the particles' pre-charge is located remote from their contact area. In this case, no charge is transferred despite different pre-charges.

However, when a pre-charge spot of one particle overlaps the contact area while the pre-charge of the other one does not, the impact charge can be much higher compared to the one predicted by the uniform model. This is due to the fact that even if the initial charge difference of the particles is not that high, their difference in charge density at the contact point is. In comparison, a uniformly charged particle exhibits at the contact area a lower charge density since the charge is distributed over the complete surface. Consequently, its charge difference at the contact area is lower.

Another important characteristic of the non-uniform model is that it may also predict an impact charge in case both particles carry an equal pre-charge. Even in this case, there can be a significant charge density difference at the contact area, which is not accounted for by the uniform model.

5.3.4. Electrostatic charging of helicopters in a dusty atmosphere [12, 13]

A helicopter flying through an atmosphere containing particulates may accumulate high electrostatic charges, which can challenge its operational safety. Despite the incomparableness of the flow, the physics underlying this charging is identical to the charging during powder transport as discussed in the remainder of this document. Thus, the author established in publications [12, 13] a side branch of his research applying the triboelectric charging model to the flight of a helicopter through an atmosphere containing particulates. Whereas before only empirical data was available, the performed investigation is highly innovative. Utilizing, for the first time, CFD to provide information concerning the electrification of an aircraft this approach allowed a detailed analysis of the location of charge accumulation.

https://doi.org/10.7795/110.20221208

In order to handle the complex geometry of the helicopter and its rotating rotor on a Cartesian grid, the author implemented the virtual boundary method [100, 101]. Therein, the solid boundary is replaced by a body force ensuring the same boundary conditions, i.e., enforcing no-slip. More specifically, the immersed boundary method proposed by Revstedt [102] and Szasz et al. [103] was employed. Therein surface meshes are generated for the solid boundaries. The body force which is added on the RHS of the momentum equation (2.1b) is given by

$$\boldsymbol{F}_{\mathrm{b}} = C_1(\boldsymbol{u}_{\mathrm{s}} - \boldsymbol{u})\mathrm{e}^{-C_2 d^2} \tag{5.3}$$

where d denotes the distance from the cell center to the surface mesh and $\boldsymbol{u}_{\mathrm{s}}$ is the velocity of the solid boundary. Accordingly, for the rotor, $\boldsymbol{u}_{\mathrm{s}}$ is equal to the sum of the flight and the local blade velocities. Thus, due to the rotation of the rotor, the value of $\boldsymbol{u}_{\mathrm{s}}$ is updated each timestep. Further, C_1 and C_2 are model constants corresponding to a relaxation factor and the spatial decay rate of the source term.

In particular, the conditions considered in Ref. [12] exposed the rotor and fuselage to a current of about 10 µA. Further, this model was used for the study of the electrification of helicopters of various configurations [13]. The examined configurations included rotor systems equipped with two, three, or four blades of various sizes and rotational frequencies. It was reported that a helicopter with fewer blades experiences less electric current even though the charge on each individual blade is higher. Further, the location of the charge build-up on the rotor disk depends strongly on the number of blades. Also, a reduction of the rotor size leads to a reduction of its electrification, even if the blade tip velocity is kept constant.

Thus, the developed numerical tool is capable of supporting the design of the electrostatic discharge system of a helicopter.

5.4. Conclusions

The question of how much charge is accumulated by a fluid/solid mixture is of utmost importance for plant safety. Therefore, exhaustive computations were performed by the author and presented in this chapter regarding a wide range of flows. Fundamental findings regard the identification of charge transport mechanisms which showed to be controlled by the interplay of turbopheresis, particle-bound charge transport, and inter-particle charge diffusion. The author demonstrated that for high particle Stokes numbers high charge is generated at the walls and transported throughout the entire channel via particle-bound charge transport, even at very low volume fractions. At intermediate Stokes numbers, the charge is efficiently distributed flow by inter-particle charge diffusion if the particle number density, particle material density or particle charge is sufficiently high. Further, a large amount of data was produced revealing the dependence of the powder charge on the conveying conditions, design parameters of the piping system and properties of the involved material. These physical insights may facilitate the prevention of electrostatic charge build-up in various technological applications, respectively the mitigation of its hazardous effects. Future research may focus on more realistic systems, i.e., non-spherical particle shapes or more complex piping geometries including rough surfaces.

6. Flow modulation through electrostatic charges

6.1. Introduction

The charge accumulation of particles effectuates the appearance of electrostatic forces which play an important role in many particle-laden flows. Examples in nature include the formation of geological patterns on Mars' surface [104] and pollen capture by plants [105]. Also, the possibility to manipulate particle dynamics through electrostatics is frequently exploited in industrial applications, e.g., in the separation of different kinds of insulating materials [106] or electrophotography [107]. As regards pure fluid flows it was pointed out by Klinkenberg and van der Minne [108] and Krämer [109] that the emerging flow pattern determines the fluid's extent of charging. In other words, the flow field of a fluid and its charging are bi-directional coupled. One may anticipate that analogously the same fact holds also for particle-laden flows.

Therefore, the availability of an accurate computational model to predict the interaction of charged particles is of great importance. However, the calculation of a charged particulate phase faces several challenges. Many of them stem from the fact that in the Lagrangian framework the computational effort scales by $O(N^2)$ with N being the number of particles [110].

As regards electrostatic forces, this can be remedied by calculation of the electric field in the Eulerian framework, i.e., through Gauss' instead of Coulomb's law which are both mathematically equivalent (cf. section 2.3). Due to its efficiency and convenience to impose boundary conditions, Gauss' law represents an attractive approach to compute real-scale systems and was used in many studies regarding particle-laden flows (e.g., in references [82, 111–113]). However, Gauss' law involves a spatial derivative (equation (2.14a)) whose numerical solution requires its discretization on a grid. This issue is critical since the electric field increases with the inverse square of their distance which means that a very fine grid is required. This problem was already tackled by Aboud et al. [114] and Hockney and Eastwood [115] for the electrostatic interactions between ions in electrolytic solutions. Nevertheless, despite some similarities, their P^3M algorithm is not suitable to treat much larger, polydisperse, and possibly heterogeneously charged particles. In order to handle these issues, the author proposed in publication [14] a new hybrid approach combining both Gauss' and Coulomb's law.

The wish to compute flows consisting of more particles motivated the development of new algorithms. Noteworthy contributions represent the recent formulations of a charged particulate phase in the Eulerian framework by Kolehmainen et al. [116] and Ray et al. [117]. These approaches are promising whereas the inclusion of short-range electrostatic forces is outstanding. A compromise between the most accurate description and computational efficiency was established by the author in publication [15] wherein the stochastic parcel method was adapted to charged particles.

The following sections outline the author's publications regarding the modulation of particle-laden flows effectuated by electrostatic charges. Section 6.2 summarizes the advancement of mathematical models in Refs. [14, 15] by the author and co-workers facilitating an accurate numerical description of the interaction of charged particles. Section 6.3 serves as an introduction to Refs. [14, 16] in which these models were employed to predict emerging flow patterns.

The results presented in this chapter were obtained in close collaboration with Prof. Dr. M. V. Papalexandris (Université catholique de Louvain, Belgium).

https://doi.org/10.7795/110.20221208

6.2. Interaction between charged particles

6.2.1. Hybrid Gauss-Coulomb approach [14]

To remedy the disadvantages of Gauss' and Coulomb's law, the author proposed a new hybrid scheme that combines both approaches. Therein, the interaction of an individual particle with the space charge, i.e., with the electric field originating from the particle cloud, is calculated via Gauss' law. As regards short-range electrostatic forces between close particles, a sub-grid model is derived based on Coulomb's law. In detail, the proposed algorithm to compute the electric field forces on a single particle *i* is as follows:

1. Derive the Eulerian charge density field from the Lagrangian particle charges (equation (2.17)).
2. Calculate the electric field at the location of particle *i* based on Gauss' law (equation (2.14a)).
3. Identify the *n* particles which reside in the same computational cell as particle *i*.
4. Solve the Coulomb interaction (equation (2.20)) between particle *i* and each of the *n* particles. Sum up the resulting electric field at the location of particle *i*.
5. Sum up the electric field obtained through steps 2 and 4 and compute the force on the particle (equation 2.13) based on this sum.

The accuracy of the numerical solution of Gauss' law, Coulomb's law, and the hybrid approach was assessed based on some characteristic length-scales. By equating the kinetic energy of a particle and its potential energy of the electric field arising from the charge of a neighboring particle, a characteristic length-scale is defined, namely

$$\lambda = \frac{3}{8\,\pi^2} \frac{Q_1\,Q_2}{\rho_\mathrm{p}\,u_0^2\,\varepsilon_0\,r_\mathrm{p}^3}\,. \tag{6.1}$$

In the case of high values of λ the repelling electrical forces are sufficiently strong to prevent the particles from colliding with each other. In contrast, if λ is small, the particles may come very close to each other and might even collide if their radii are sufficiently large. This relation is quantified by a new non-dimensional number given by

$$\chi = 2\,r_\mathrm{p}/\lambda\,. \tag{6.2}$$

Thus, electric forces are important for particle interaction dynamics if both λ and χ are sufficiently small. On the contrary, if χ is large inertia and collisions are dominating whereas for large λ the electric forces prevent particle approaches. Further, the grid resolution for solving Gauss' law, *h*, is expressed through a second non-dimensional parameter,

$$\chi_h = h/\lambda\,. \tag{6.3}$$

Computations concerning binary charged particle interactions in a vacuum and absence of gravitational forces are visualized in figure 6.1. The two particles ($\rho_\mathrm{p} = 4000\,\mathrm{kg/m^3}$, $r_\mathrm{p} = 250\,\mu\mathrm{m}$, $Q = 100$ pC) were initially placed 10 mm apart and accelerated with $u_0 = 0.5$ m/s towards each other along the *x*-axis of the coordinate system. Since the motion of both particles is symmetric with respect to the origin at $x = 0$, the trajectory for only one particle is given. Further, the abscissa in figure 6.1 gives the time multiplied by the initial particle velocity. The difference in the depicted cases lies in the applied grid to solve Gauss' law. In case 1 uniform cells of a spacing of $\chi_h = 0.72$ were employed whereas in case 6 the grid was refined to $\chi_h = 0.36$.

https://doi.org/10.7795/110.20221208

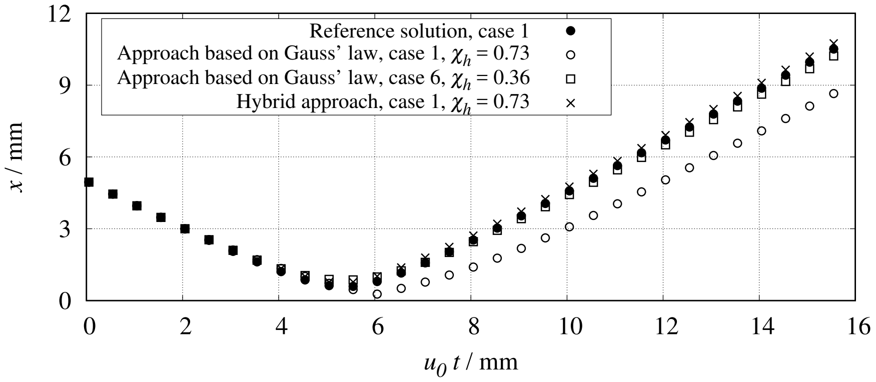

Figure 6.1.: Trajectory of a particle during binary particle interactions predicted by Coulomb's law (reference solution), Gauss' law, and the new hybrid approach. The Gauss' law solution was computed on two different grid resolutions, $\chi_h = 0.72$ and $\chi_h = 0.36$ (reprinted with permission from Ref. [14]).

According to the trajectory calculated from Coulomb's law (which is denoted *reference solution* in figure 6.1) the particles approach each other due to their initial momentum. When they come sufficiently close, then the electrostatic forces become strong and finally the particles repel each other. It can be observed that the trajectory predicted by the numerical solution of Gauss' law on the coarse grid is qualitatively different from the exact reference solution. This difference is related to the electric field being under-resolved which introduces a significant numerical error. This error even leads to the prediction of an unphysical collision at $u_0 t = 6.0$ mm when using Gauss' law.

In contrast, the results of the newly proposed hybrid approach are very similar to those of Coulomb's law. The small discrepancy between both solutions observable in figure 6.1 is caused when both particles are close to each other but located in an adjacent cell, i.e., in a region of a badly resolved electric field. However, if the grid is refined to $\chi_h = 0.36$ the accuracy of Gauss' law solution is significantly improved. In particular, using this resolution the unphysical particle collision is not predicted any longer. It is noteworthy that for these conditions the hybrid approach gives a similar accuracy than Gauss' law while it requires eight times less computational cells. Thus, the hybrid approach provides a computationally cheap alternative to approaches based on Coulomb's or Gauss' laws.

Further, the author explored how the numerical errors of the three considered approaches scale with respect to the non-dimensional parameters χ and χ_h. To this end, a measure of the numerical error based on the rms of the error of the particle locations at each time instance, i.e.,

$$e_{\mathrm{rms}} = \left(\frac{\int_0^{\Delta t} |\boldsymbol{x}_{\mathrm{C}} - \boldsymbol{x}|^2 \, dt}{\Delta t} \right)^{1/2} \tag{6.4}$$

was employed. In the above equation, $\boldsymbol{x}_{\mathrm{C}}$ is the "exact" solution, i.e., the one computed from Coulomb's law and $\boldsymbol{x}$ is the solution computed either via Gauss' law or the new hybrid approach. The computation length, Δt, covered the complete interaction between the two particles.

In figure 6.2, this error measure is plotted for a fixed χ_h of 0.73 and varying χ. A filled symbol denotes that a collision was predicted by the respective numerical method whereas an open symbol means that no collision was predicted. Further, in case the collision was predicted correctly, the symbol is filled black, if not, it is filled red. It is inferred from figure 6.2 that

https://doi.org/10.7795/110.20221208

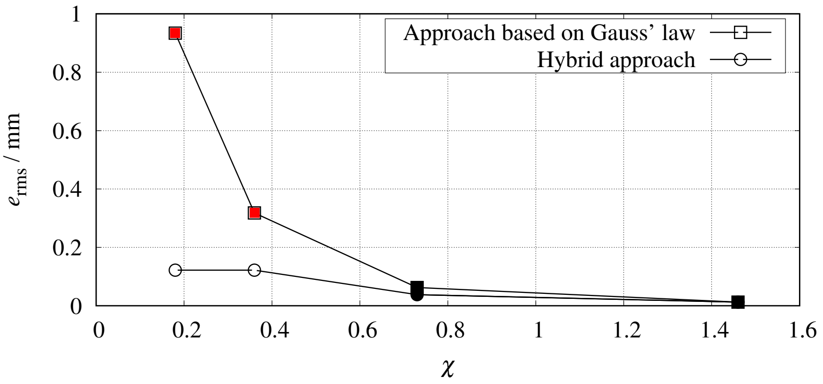

Figure 6.2.: Numerical errors of the hybrid approach and the approach based on Gauss' law for cases with fixed $\chi_h = 0.73$ and variable χ. The filled symbols represent cases where a collision occurs, the empty symbols where no collision occurs. Symbols filled with a red color mark cases where a collision was erroneously predicted by the respective method (reprinted with permission from Ref. [14]).

non-physical collisions occurred when using Gauss' law for $\chi = 0.18$ and 0.36. In these cases, the error of the hybrid approach, which predicts accurately that no collisions take place, is much smaller. However, for large values of χ the particle dynamics is collision dominated and the accurate representation of the electric field is less important. Thus, the error of both the hybrid approach and Gauss' law drops significantly. To sum up, the hybrid approach is in particular superior over Gauss' law in the case of low χ.

6.2.2. Stochastic parcel model [15]

As stated in the introduction of this chapter, a general drawback of Lagrangian particle tracking is that the computational effort scales with the square of the present particles. In order to facilitate the treatment of a larger amount of particles the author described in reference [15] the particulate phase in terms of the particle number density function (cf. equation(2.5)). This function was discretized in computational parcels, each parcel representing a number of particles (ζ) and tracked in a Lagrangian framework.

With respect to acceleration during collisions, a statistical technique that yields a collision frequency is employed [98]. More specifically, it is assumed that the probability P_n that the particles of parcel n collide with the particles of parcel m during the time increment dt follows a Poisson distribution, namely

$$P_n = 1 - \mathrm{e}^{-\omega_{nm}\,dt}\,. \tag{6.5}$$

In this equation, the time-averaged collision frequency ω_{nm} is defined as

$$\omega_{nm} = \pi \frac{\zeta_m \left(r_{\mathrm{p},n} + r_{\mathrm{p},m}\right)^2 |\boldsymbol{u}_{\mathrm{p},n} - \boldsymbol{u}_{\mathrm{p},m}|}{(\boldsymbol{e}_x \cdot \boldsymbol{\delta})(\boldsymbol{e}_y \cdot \boldsymbol{\delta})(\boldsymbol{e}_z \cdot \boldsymbol{\delta})} \tag{6.6}$$

where $\boldsymbol{\delta}$ is a vector pointing from the location of one parcel to the other, $\boldsymbol{e}_x$, $\boldsymbol{e}_y$ and $\boldsymbol{e}_z$ denote the unit vectors of the Cartesian coordinate system and $\cdot$ the scalar product.

Using the particle number density function, the electric charge density which is needed to solve Gauss' law reads

$$\int_{\mathscr{V}} \rho_{\mathrm{el}}\,\mathrm{d}\mathscr{V} \;=\; \sum_{m=1}^{N} \zeta_m Q_m\,, \tag{6.7}$$

https://doi.org/10.7795/110.20221208

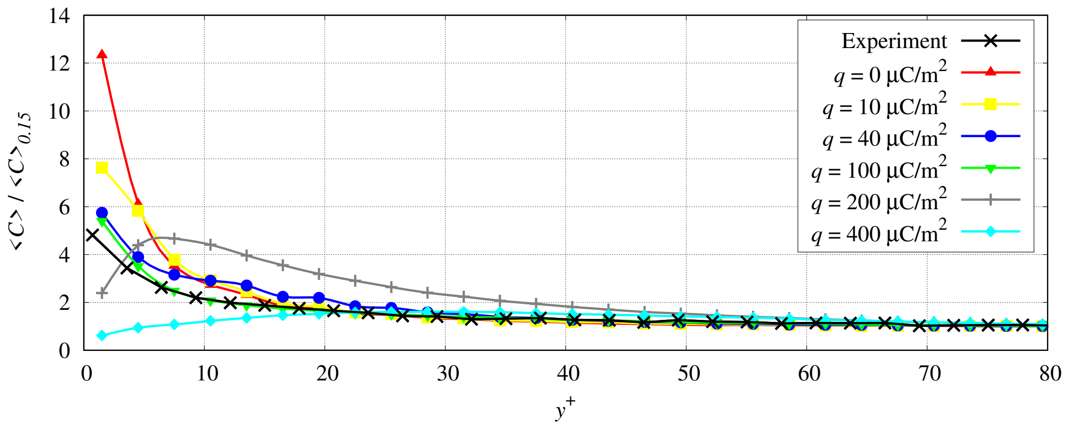

Figure 6.3.: Comparison of the measured and simulated mean particle concentration distribution in the near-wall region. The local concentration is normalized by the mean concentration at $y = 0.15\,H$. Note that the plotted data is collected along the laser beam (cf. Villafañe et al. [118]), i.e., the respective z^+ position varies with the y^+ coordinate (reprinted with permission from Ref. [15]).

where $\mathscr{V}$ is a control volume containing N parcels. Further, Coulomb's law becomes

$$\boldsymbol{E}(\boldsymbol{r}) = \frac{\zeta_m\, Q_m\, \boldsymbol{r}}{4\,\pi\,\varepsilon_0\,|\boldsymbol{r}|^3}\,. \tag{6.8}$$

where $\boldsymbol{E}(\boldsymbol{r})$ is the electric field a particle is subjected to due to the presence of another parcel consisting of ζ_m particles carrying the charge Q_m.

6.3. Emerging flow patterns [15, 16]

The models presented in the previous section were implemented by the author to investigate the pattern of turbulent particle-laden flows under the influence of electrostatic charges. These investigations were conducted in a generic computational domain representing a square-shaped duct of a side length of $2H$. The Reynolds number of the gas flow was 10 000 based on the bulk flow velocity and H, respectively 600 on the friction velocity. In the streamwise direction, the computational domain extends $15H$ and periodic boundary conditions were chosen in order to mimic an infinite duct length. The particles' charge was fixed, i.e., no charge is exchanged during collisions with the walls or in-between particles.

The results of the simulations were compared to experimental data obtained by Dr. L. Villafañe in a flow facility at Stanford University. The test-rig consists of a 5.4 m long smooth aluminum duct with a 40 mm wide cross-section which ensures a fully developed turbulent airflow at the glass test section where measurements are reported. Further details concerning the facility are to be found in Refs. [16, 118]. It is suspected that the particles in the experiment accumulate electrostatic charge while being transported through the piping system which is corroborated by the formation of deposit layers at the glass windows. The amount of charge is, however, unknown. Therefore, the author conducted a parametric study considering six different charge density values between $q = 10$ µC/m and $q = 400$ µC/m^2. The particle size distribution resembled the characteristics of the powder batch used in the experiment.

The resulting mean particle concentrations normalized by the mean concentration at $y = 0.15\ H$ are visualized for the near-wall region in figure 6.3. The profiles are plotted along

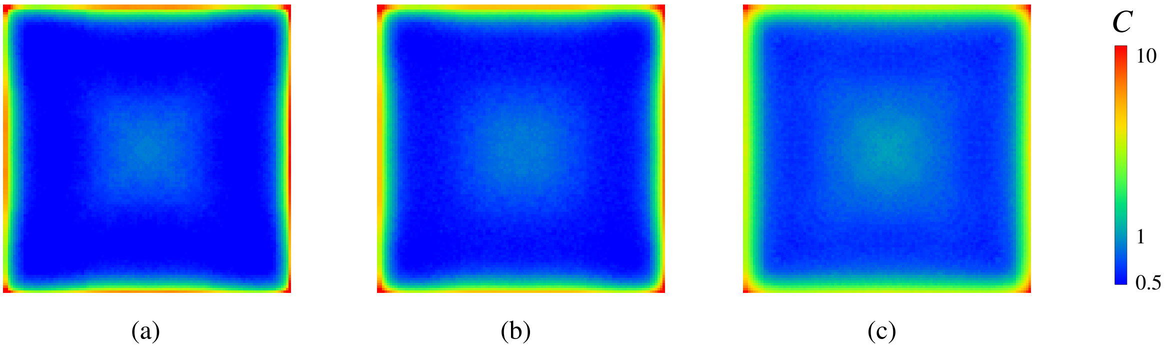

(a) (b) (c)

Figure 6.4.: Logarithmic representation of the mean normalized particle concentration in the duct cross-section, (a) Q =0 pC, (b) Q = 0.125 pC and (c) Q = 0.25 pC (reprinted with permission from Ref. [16]).

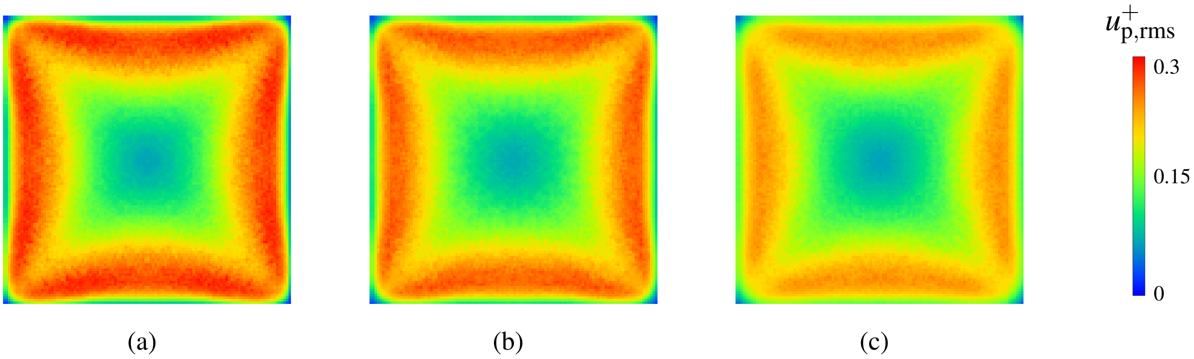

(a) (b) (c)

Figure 6.5.: Fluctuations of the streamwise particle velocity in the duct cross-section, (a) Q =0 pC, (b) Q = 0.125 pC and (c) Q = 0.25 pC (reprinted with permission from Ref. [16]).

the laser sheet centerline in the experimental setting which was inclined by 18° with respect to the wall-normal. The differences in the numerical results reveal the potential influence of electrostatic charges on preferential particle concentration especially in the vicinity of the wall. A comparison of the data suggests that the case corresponding to $q = 100$ µC/m^2 replicates the closest the experimental measurements. The remaining discrepancies can be attributed to the crude assumptions underlying the charge distribution, the boundary conditions to the electric field, or the details of the data acquisition in the experiment (see Grosshans et al. [15] for a detailed discussion).

In order to obtain results of more fundamental relevance, a batch of monodisperse particles of a diameter of $1.25\times10^{-3}H$ and of a material density of 7500 times the gas density was considered. The considered flow was dilute of a solid-gas mass loading ratio of 0.01. Three simulations were run and the particles of each simulation were equally charged, either with zero charge, $Q = 0.125$ pC or $Q = 0.25$ pC. The resulting average particle concentrations over the duct cross-section are plotted in figure 6.4. These profiles are averaged in the streamwise direction and over the eight symmetric triangles of the duct-cross section and normalized with the mean concentration in the duct.

The results evidence the phenomenon of *turbophoreses*, i.e., particle accumulation in the vicinity of the walls and especially in the corners of the duct. Comparing figures 6.4(a), 6.4(b)

https://doi.org/10.7795/110.20221208

and 6.4(c) reveals that electrostatic forces have the highest influence on the particle concentrations in the viscous wall region and close to the wall symmetry lines. More specifically the particles are distributed the more homogeneously the higher their charge is. In other words, the concentration gradients in the near-wall region and the peaks at the corners are reduced if the particles' charge is increased. Also, the particle concentration peaks at the wall bisector (i.e., the centerline of each wall), which is affected by outward crossflows and secondary flows. These peaks are dampened when charge is assigned to the particles and even vanish in case of a charge of $Q = 0.25$ pC.

For further analysis of the flow patterns, the streamwise particle velocity fluctuations fields are plotted in figure 6.5. The relatively high flow Stokes number leads to an approximately one order lower magnitude of these fluctuations than the respective gas phase fluctuations. Moreover, the plotted fields demonstrate the dampening of fluctuations effectuated by the assigned charge. This effect is related to repelling forces in-between particles. Through that, electrical forces counteract aerodynamic instabilities and cause a stabilizing effect for the particle trajectories. Also, the inter-particle collision frequency is reduced by repelling electrical forces which further reduces velocity fluctuations.

6.4. Conclusions

The amount of charging of particle-laden flows strongly depends on the pattern of the flow. The flow pattern is, in turn, affected by electrostatic forces if the accumulated charge is sufficiently high. In order to explore the interaction between charged particles, the author proposed a hybrid approach combining the numerical advantages of Coulomb's and Gauss' law. For large particle systems, the new scheme is computationally more efficient than solving Coulomb's law alone, whereas it is eight times faster than solving Gauss' law with the same accuracy. This new approach was utilized to investigate the arising flow pattern of powder in a duct of a squared cross-section. The results corroborated that charge counteracts particle accumulation at the walls and affects a more homogeneously distributed particulate phase. Also, electrostatic forces stabilized the flow through dampening the particle velocity fluctuations. These findings enable to a certain extent the control of particle-laden flows and contribute to the understanding of charge transport in duct flows. Thus far, the study was limited to particles of equal polarities and repelling inter-particle forces. It is expected that the consideration of charges of different polarity as well as the inclusion of induced charges on the particles' surface will shed light on interesting fundamental questions of EHD particulate flows. Also, the possible modulation of the statistical properties of the fluid through electrostatic forces is a topic worth investigating.

7. Perspectives

In the document in hand, the author's scientific contributions to the field of computation of particle production, particle-laden flows and particle electrification are summarized. While the achievements and progress in terms of numerical modeling were presented in the previous chapters, in this last section an outlook on the future directions of this research field shall be given.

Fundamentally, this topic involves the solution of the Navier-Stokes equations for the fluids, Newton's laws of motion for the particles, and Maxwell's equations for the electric field. Even though their mathematical formulations are well-established, they might be challenging to solve. Thus, it is the author's opinion that the most important issues to be tackled in the future are related to physical mechanisms which are not covered by these equations. Most often, for this kind of mechanisms so far only empirical models or solutions for very limited conditions are available whereas generally valid approaches are lacking. For example, the accuracy of the prediction of the particles' shapes and morphologies is still not satisfactory considering the importance for the usability of powders. Further, an important uncertainty in the mathematical description of the triboelectric charging of particulate flows is the precise prediction of the amount of exchanged charge during single particle-wall and particle-particle contacts. Despite the complexity of the problem, the advancement of single-particle experiments and theoretical models on a molecular basis may guide the path for the improvement of CFD models. Also, the coupling of the fluid, particulate, and electric equations to compute flow patterns affected by electrostatic forces is currently limited to specific situations. Therefore, the development of approaches that are valid for different charges and polarities as well as computationally efficient Eulerian formulations for the particulate phase is of high interest.

In the future, the author aims to approach these issues through a newly developed computational tool, pafiX [119] (particle flow simulation in eXplosion protection). Essentially, this tool is based on the outcome and development outlined in the present manuscript.

https://doi.org/10.7795/110.20221208

8. Bibliography

[1] Grosshans, H., Griesing, M., Mönckedieck, M., Hellwig, T., Walther, B., Gopireddy, S. R., Sedelmayer, R., Pauer, W., Moritz, H.-U., Urbanetz, N. A., and Gutheil, E. (2016). *Numerical and experimental study of the drying of bi-component droplets under various drying conditions*. Int. J. Heat Mass Transfer, 96:97–109.

[2] Grosshans, H., Griesing, M., Hellwig, T., Pauer, W., Moritz, H.-U., and Gutheil, E. (2016). *A new model for the drying of mannitol-water droplets in hot air above the boiling temperature*. Powder Technol., 297:259–265.

[3] Grosshans, H., Gopireddy, S. R., and Gutheil, E. (2014). *Numerical simulation of PVP-water sprays under various injection conditions*. In *ILASS – Europe 2014, 26th Ann. Conf. Liquid Atomiz. Spray Syst., 8-10 Sep. 2014, Bremen, Germany*.

[4] Grosshans, H., Gopireddy, S. R., Humza, R. M., and Gutheil, E. (2016). *Modeling and simulation of single particle and spray drying of PVP- and mannitol-water in hot air*. In Fritsching, U., editor, *Process-Spray: Functional Particles Produced in Spray Processes*, Springer Science & Business Media. Springer International Publishing.

[5] Grosshans, H. and Papalexandris, M. V. (2016). *A model for the non-uniform contact charging of particles*. Powder Technol., 305:518–527.

[6] Grosshans, H. and Papalexandris, M. V. (2017). *Direct numerical simulation of triboelectric charging in a particle-laden turbulent channel flow*. J. Fluid Mech., 818:465–491.

[7] Grosshans, H. and Papalexandris, M. V. (2018). *Exploring the mechanism of inter-particle charge diffusion*. Eur. Phys. J. Appl. Phys., 82(1):11101.

[8] Grosshans, H. and Papalexandris, M. V. (2016). *Large eddy simulation of triboelectric charging in pneumatic powder transport*. Powder Technol., 301:1008–1015.

[9] Grosshans, H. and Papalexandris, M. V. (2016). *Evaluation of the parameters influencing electrostatic charging of powder in a pipe flow*. J. Loss Prev. Process Ind., 43:83–91.

[10] Grosshans, H. and Papalexandris, M. V. (2017). *Numerical study of the influence of the powder and pipe properties on electrical charging during pneumatic conveying*. Powder Technol., 315:227–235.

[11] Schwindt, N., von Pidoll, U., Markus, D., Klausmeyer, U., Papalexandris, M. V., and Grosshans, H. (2017). *Measurement of electrostatic charging during pneumatic conveying of powders*. J. Loss Prev. Process Ind., 49:461–471.

[12] Grosshans, H., Szász, R.-Z., and Papalexandris, M. V. (2017). *Modeling the electrostatic charging of a helicopter during hovering in dusty atmosphere*. Aerosp. Sci. Technol., 64:31–38.

[13] Grosshans, H., Szász, R.-Z., and Papalexandris, M. V. (2018). *Influence of the rotor configuration on the electrostatic charging of helicopters*. AIAA J., 56:368–375.

[14] Grosshans, H. and Papalexandris, M. V. (2017). *On the accuracy of the numerical computation of the electrostatic forces between charged particles*. Powder Technol., 322:185–194.

[15] Grosshans, H., Villafañe, L., Banko, A., and Papalexandris, M. V. (2019). *Case study on the influence of electrostatic charges on particle concentration in turbulent duct flows*. Powder Technol., 357:46–53.

[16] Grosshans, H. (2018). *Modulation of particle dynamics in dilute duct flows by electrostatic charges*. Phys. Fluids, 30(8):083303.

https://doi.org/10.7795/110.20221208

[17] Richardson, L. F. (1922). *Weather Prediction by Numerical Process*. Cambridge University Press.

[18] Leslie, D. C. and Quarini, G. L. (1979). *The application of turbulence theory to the formulation of subgrid modelling procedures*. J. Fluid Mech., 91:65–91.

[19] Pope, S. B. (2000). *Turbulent Flows*. Cambridge University Press.

[20] Taylor, S. G. I. (1935). *Statistical theory of turbulence*. Proc. R. Soc. London, Ser. A, Math. Phys. Sci., 151(873):421–444.

[21] Smagorinsky, J. (1963). *General circulation experiments with the primitive equations: I. The basic equations*. Mon. Weather Rev., 91:99–164.

[22] Germano, M., Piomelli, U., Moin, P., and Cabot, W. H. (1991). *A dynamic subgrid-scale eddy viscosity model*. Phys. Fluids A, 3(7):1760–1765.

[23] Bardina, J., Ferziger, H., and Reynolds, W. C. (1980). *Improved subgrid models for large eddy simulation*. AIAA Paper, 80(1357).

[24] Liu, S., Meneveau, C., and Katz, J. (1994). *On the properties of similarity subgrid-scale models as deduced from measurements in a turbulent jet*. J. Fluid Mech., 275:83–119.

[25] Boris, J. P., Grinstein, F. F., Oran, E. S., and Kolbe, R. L. (1992). *New insights into large eddy simulation*. Fluid Dyn. Res., 10:199–228.

[26] Baldwin, B. S. and Lomax, H. (1978). *Thin-layer approximation and algebraic model for seperated turbulent flow*. AIAA Paper, 78(257).

[27] Jones, W. P. and Launder, B. E. (1972). *The prediction of laminarization with a two-equation model of turbulence*. Int. J. Heat Mass Transfer, 15:301–314.

[28] Wilcox, D. C. (1998). *Turbulence Modeling for CFD*. DCW Industries, 2nd edition.

[29] Williams, F. A. (1958). *Spray combustion and atomization*. Phys. Fluids (1958-1988), 1(6):541–545.

[30] Crowe, C., Schwarzkopf, J. D., Sommerfeld, M., and Tsuji, Y. (2012). *Multiphase Flows with Droplets and Particles*. CRC Press, Boka Raton, FL, second edition.

[31] Schiller, L. and Naumann, A. Z. (1933). *A drag coefficient correlation*. Z. Ver. Dtsch. Ing., 77:318–320.

[32] Maxey, M. R. and Riley, J. J. (1983). *Equation of motion for a small rigid sphere in a nonuniform flow*. Phys. Fluids, 26:883–889.

[33] Grosshans, H. (2013). *Large Eddy Simulation of Atomizing Sprays*. Ph.D. thesis, Lund University.

[34] Priego-Capote, F. and de Castro, L. (2006). *Ultrasound-assisted levitation: Lab-on-a-drop*. Trends Anal. Chem., 25(9):856–867.

[35] Trinh, E. H. and Robey, J. L. (1994). *Experimental study of streaming flows associated with ultrasonic levitators*. Phys. Fluids, 6(11):3567.

[36] Kawahara, N., Yarin, A. L., Brenn, G., Kastner, O., and Durst, F. (2000). *Effect of acoustic streaming on the mass transfer from a sublimating sphere*. Phys. Fluids, 12(4):912.

[37] Yarin, A. L., Brenn, G., Kastner, O., Rensink, D., and Tropea, C. (1999). *Evaporation of acoustically levitated droplets*. J. Fluid Mech., 399:151–204.

[38] Yan, Z. L., Xie, W. J., and Wei, B. (2011). *Vortex flow in acoustically levitated drops*. Physics Letters A, 375(37):3306–3309.

[39] Abramzon, B. and Sirignano, W. A. (1989). *Droplet vaporization model for spray combustion calculations*. Int. J. Heat Mass Transfer, 32(9):1605–1618.

[40] Nešić, S. (1989). *The evaporation of single droplets – experiments and modelling*. Drying, 89:386–393.

https://doi.org/10.7795/110.20221208

[41] Farid, M. (2003). *A new approach to modelling of single droplet drying*. Chem. Eng. Sci., 58(13):2985–2993.

[42] Charlesworth, D. H. and Marshall, W. R. (1960). *Evaporation from drops containing dissolved solids*. AIChE J., 6(1):9–23.

[43] Sano, Y. and Keey, R. B. (1982). *The drying of a spherical particle containing colloidal material into a hollow sphere*. Chem. Eng. Sci., 37(6):881–889.

[44] Brenn, G. (2004). *Concentration fields in drying droplets*. Chem. Eng. & Technol., 27(12):1252–1258.

[45] Walton, D. E. (2000). *The morphology of spray-dried particles a qualitative view*. Drying Technol., 18(9):1943–1986.

[46] Vicente, J., Pinto, J., Menezes, J., and Gaspar, F. (2013). *Fundamental analysis of particle formation in spray drying*. Powder Technol., 247(0):1–7.

[47] Mezhericher, M., Levy, A., and Borde, I. (2010). *Theoretical models of single droplet drying kinetics: A review*. Drying Technol., 28(2):278–293.

[48] Dukowicz, J. K. (1980). *A particle-fluid numerical model for liquid sprays*. J. Comput. Phys., 35(2):229–253.

[49] Marchisio, D. L., Pikturna, J. T., Fox, R. O., Vigil, R. D., and Barresi, A. A. (2003). *Quadrature method of moments for population-balance equations*. AIChE Journal, 49(5):1266–1276.

[50] McGraw, R. (1997). *Description of aerosol dynamics by the quadrature method of moments*. Aerosol Sci. Technol., 27(2):255–265.

[51] Marchisio, D. L. and Fox, R. O. (2005). *Solution of population balance equations using the direct quadrature method of moments*. J. Aerosol Sci., 36(1):43–73.

[52] Fox, R. O., Laurent, F., and Massot, M. (2008). *Numerical simulation of spray coalescence in an eulerian framework: Direct quadrature method of moments and multi-fluid method*. J. Comput. Phys., 227(6):3058–3088.

[53] Dolinski, A. A. and Ivanicki, G. K. (1984). *Optimisation of the processes of spray drying*. Naukova Dumka, Kiev, USSR.

[54] Nešić, S. and Vodnik, J. (1991). *Kinetics of droplet evaporation*. Chem. Eng. Sci., 46(2):527–537.

[55] Gopireddy, S. R. and Gutheil, E. (2013). *Numerical simulation of evaporation and drying of a bi-component droplet*. Int. J. Heat Mass Transfer, 66:404–411.

[56] Kelly, P. (2013). *Solid Mechanics Part I: An Introduction to Solid Mechanics*. Solid Mechanics Lecture Notes. University of Auckland.

[57] Grote, K.-H. and Feldhusen, J. (2007). *Dubbel*. Springer, Wiesbaden Berlin Heidelberg. ISBN 978-3-540-68191-5.

[58] Griesing, M. (2016). *Untersuchung der Trocknungskinetik und Strukturbildung von Vinylacetat-Ethylen-Copolymerdispersionen in akustisch levitierten Einzeltropfen*. Ph.D. thesis, University of Hamburg.

[59] Hellwig, T. (2018). *Acoustic Levitation as an analytical methodfor the investigation of multicomponent droplets*. Ph.D. thesis, University of Hamburg.

[60] Gopireddy, S. R., Humza, R. M., Wimmer, E., Brenn, G., and Gutheil, E. (2014). *Modelling and simulation of water and PVP/water evaporating spray flows using the direct quadrature method of moments*. Atomization Sprays, 24(5):403–429.

[61] Villedieu, P. and Hylkema, J. (1997). *Une méthode particulaire aléatoire reposant sur une équation cinétique pour la simulation numérique des sprays denses de gouttelettes liquides*. C. R. Acad. Sci. Ser. I: Math., 325(3):323–328.

https://doi.org/10.7795/110.20221208

[62] Laurent, F., Massot, M., and Villedieu, P. (2004). *Eulerian multi-fluid modeling for the numerical simulation of coalescence in polydisperse dense liquid sprays*. J. Comput. Phys., 194(2):505–543.

[63] Launder, B. E. and Sharma, B. I. (1974). *Application of the energy dissipation model of turbulence to the calculation of flow near a spinning disc*. Lett. Heat Mass Transfer, 1:131–138.

[64] Wimmer, E. and Brenn, G. (2013). *Vermessung von Polymerlösungssprays aus einem Drall-Druck-Zerstäuber*. Technical report, Institute of Fluid Mechanics and Heat Transfer, TU Graz.

[65] Saffman, M. (1987). *Automatic calibration of lda measurement volume size*. Appl. Optics, 26:2592–2597.

[66] Tratnig, A. (2009). *Characteristics of Sprays Produced by Pressure-Swirl Atomizers*. Ph.D. thesis, TU Graz.

[67] Tratnig, A. and Brenn, G. (2010). *Drop size spectra in sprays from pressure-swirl atomizers*. International Journal of Multiphase Flow, 36(5):349–363.

[68] Walzel, P. (2011). *Influence of the spray method on product quality and morphology in spray drying*. Chem. Eng. & Technol., 34(7):1039–1048.

[69] Faeth, G. M., Hsiang, L.-P., and Wu, P. K. (1995). *Structure and breakup properties of sprays*. Int. J. Multiphase Flow, 21:99–127.

[70] Elkotb, M. M. (1982). *Fuel atomization for spray modelling*. Prog. Energy Combust. Sci, 8:61–91.

[71] Lin, S. P. and Reitz, R. D. (1998). *Drop and spray formation from a liquid jet*. Annu. Rev. Fluid Mech., 30:85–105.

[72] Lacks, D. J. (2012). *The unpredictability of electrostatic charging*. Angew. Chemie Int. Ed., 51:6822–6823.

[73] Ireland, P. (2008). *The role of changing contact in sliding triboelectrification*. J. Phys. D: Appl. Phys., 41:025305.

[74] Qin, J., Li, J., Lee, V., Jaeger, H., de Pablo, J. J., and Freed, K. F. (2016). *A theory of interactions between polarizable dielectric spheres*. J. Colloid Interface Sci., 469:237–241.

[75] Nomura, T., Satoh, T., and Masuda, H. (2003). *The environment humidity effect on the tribo-charge of powder*. Powder Technol., 135-136:43–49.

[76] Masui, N. and Murata, Y. (1983). *Electrification of polymer particles by impact on a metal plate*. Jpn. J. Appl. Phys., 22:1057–1062.

[77] Yamamoto, H. and Scarlett, B. (1986). *Triboelectric charging of polymer particles by impact*. Part. Charact., 3:117–121.

[78] Watanabe, H., Samimi, A., Ding, Y. L., Ghadiri, M., Matsuyama, T., and Pitt, K. G. (2006). *Measurement of charge transfer due to single particle impact*. Part. Part. Syst. Char., 23:133–137.

[79] Matsuyama, T., Ogu, M., Yamamoto, H., Marijnissen, J. C. M., and Scarlett, B. (2003). *Impact charging experiments with single particles of hundred micrometre size*. Powder Technol., 135–136:14–22.

[80] Soo, S. L. (1971). *Dynamics of charged suspensions*. In *Topics in Current Aerosol Research*, pages 71–73. Pergamon Press.

[81] John, W., Reischl, G., and Devor, W. (1980). *Charge transfer to metal surfaces from bouncing aerosol particles*. J. Aerosol Sci., 11(2):115–138.

[82] Kolniak, P. Z. and Kuczynski, R. (1989). *Numerical modeling of powder electrification in pneumatic transport*. J. Electrostat., 23:421–430.

https://doi.org/10.7795/110.20221208

[83] Matsuyama, T. and Yamamoto, H. (1995). *Electrification of single polymer particles by successive impacts with metal targets*. IEEE Trans. Ind. Appl., 31:1441–1445.

[84] Paschen, F. (1889). *Ueber die zum Funkenübergang in Luft, Wasserstoff und Kohlensäure bei verschiedenen Drucken erforderliche Potentialdifferenz*. Ann. Phys., 273:69–96.

[85] Matsuyama, T. and Yamamoto, H. (2006). *Montecarlo simulation of charge accumulating process of a single particle due to successive impact*. J. Soc. Powder Technol. Jpn., 43:169–173.

[86] Shen, X., Wang, A. E., Sankaran, R. M., and Lacks, D. J. (2016). *First-principles calculation of contact electrification and validation by experiment*. J. Electrostat., 71:11–16.

[87] Masuda, H., Komatsu, T., and Iinoya, K. (1976). *The static electrification of particles in gas-solids pipe flow*. AIChE J., 22:558–564.

[88] Artana, G., Touchard, G., and Morin, M. F. (1997). *Contribution to the analysis of the flow electrification process of powders in pneumatic conveyers*. J. Electrostatics, 40-41:277–282.

[89] Tanoue, K., Tanaka, H., Kitano, H., and Masuda, H. (2001). *Numerical simulation of tribo-electrification of particles in a gas-solid two-phase flow*. Powder Technol., 118:121–129.

[90] Nifuku, M. and Katoh, H. (2003). *A study on the static electrification of powders during pneumatic transportation and the ignition of dust cloud*. Powder Technol., 135–136:234–242.

[91] Watano, S., Saito, S., and Suzuki, T. (2003). *Numerical simulation of electrostatic charge in powder pneumatic conveying process*. Powder Technol., 135–136:112–117.

[92] Watano, S. (2006). *Mechanism and control of electrification in pneumatic conveying of powders*. Chem. Eng. Sci., 61:2271–2278.

[93] Fath, W., Blum, C., Glor, M., and Walther, C.-D. (2013). *Electrostatic ignition hazards due to pneumatic transport of flammable powders through insulating or dissipative tubes and hoses – new experiments and calculations*. J. Electrostat., 71(3):377–382.

[94] Tanoue, K., Ema, A., and Masuda, H. (1999). *Effect of material transfer and work hardening of metal surface on the current generated by impact of particle*. J. Chem. Eng. Jpn., 32:544–548.

[95] Lim, E. W. C., Yao, J., and Zhao, Y. (2012). *Pneumatic transport of granular materials with electrostatic effects*. AIChE J., 58(4):1040–1059.

[96] Tanoue, K., Ema, A., and Masuda, H. (2006). *Analysis of developing behavior in two-component development system by large-scale discrete element method*. J. Chem. Eng. Jpn., 39:1137–1144.

[97] McLaughlin, J. B. (1989). *Aerosol particle deposition in numerically simulated channel flow*. Phys. Fluids, 1:1211–1224.

[98] Stiesch, G. (2003). *Modeling Engine Spray and Combustion Processes*. Springer Verlag, Berlin Heidelberg New York.

[99] Lilly, D. K. (1992). *A proposed modification of the Germano subgrid-scale closure method*. Phys. Fluids A, 4(3):633–635.

[100] Goldstein, D., Handler, R., and Sirovich, L. (1993). *Modeling a no-slip flow boundary with an external force field*. J. Comput. Phys., 105:354–366.

[101] Revstedt, J. and Fuchs, L. (2001). *Handling complex boundaries on a Cartesian grid using surface singularities*. Int. J. Num. Meth. Fluids., 35:125–150.

[102] Revstedt, J. (2013). *Interaction between an incompressible flow and elastic cantilevers of circular cross-section*. Int. J. Heat Fluid Flow, 43:244–250.

https://doi.org/10.7795/110.20221208

[103] Szasz, R.-Z., Ronnfors, M., and Revstedt, J. (2016). *Influence of ice accretion on the noise generated by an airfoil section*. Int. J. Heat Fluid Flow, 62, Part A:83–92.

[104] Shinbrot, T., LaMarche, K., and Glasser, B. J. (2006). *Triboelectrification and razorbacks: Geophysical patterns produced in dry grains*. Phys. Rev. Lett., 96:178002.

[105] Bowker, G. E. and Crenshaw, H. C. (2007). *Electrostatic forces in wind-pollination–part 1: Measurement of the electrostatic charge on pollen*. Atmos. Environ., 41:1587–1595.

[106] Laurentie, J. C., Traoré, P., and Dascalescu, L. (2013). *Discrete element modeling of triboelectric charging of insulating materials in vibrated granular beds*. J. Electrostat., 71(6):951–957.

[107] Schein, L. B. (1999). *Recent advances in our understanding of toner charging*. J. Electrostat., 46:29–36.

[108] Klinkenberg, A. and van der Minne, J. L. (1958). *Electrostatics in the Petroleum Industry*. Elsevier Publ. Co.

[109] Krämer, H. (1983). *Kriterien zur Beurteilung der Zündgefahren infolge elektrostatisch aufgeladener Flüssigkeiten*. Chem. Ing. Tech., 55:419–428.

[110] Lapenta, G. (2013). *Particle In Cell Methods With Application to Simulations in Space Weather*. Citeseer, Astrofysica, Centrum Voor Plasma.

[111] Dastoori, K., Makin, B., Kolhe, M., Des-Roseaux, M., and Conneely, M. (2013). *CFD modelling of flue gas particulates in a biomass fired stove with electrostatic precipitation*. J. Electrostat., 71:351–356.

[112] Arif, S., Branken, D. J., Everson, R. C., Neomagus, H. W. J. P., le Grange, L. A., and Arif, A. (2016). *CFD modeling of particle charging and collection in electrostatic precipitators*. J. Electrostatics, 84:10–22.

[113] Labair, H., Touhami, S., Tilmatine, A., Hadjeri, S., Medles, K., and Dascalescu, L. (2017). *Study of charged particles trajectories in free-fall electrostatic separators*. J. Electrostatics, 88:10–14.

[114] Aboud, S., Marreiro, D., and Saraniti, M. (2004). *A Poisson P^3M force field scheme for particle-based simulations of ionic liquids*. J. Comput. Electron., 3:117–133.

[115] Hockney, R. W. and Eastwood, J. W. (1981). *Computer Simulation Using Particles*. McGraw-Hill.

[116] Kolehmainen, J., Ozel, A., and Sundaresan, S. (2018). *Eulerian modelling of gas–solid flows with triboelectric charging*. J. Fluid Mech., 848:340–369.

[117] Ray, M., Chowdhury, F., Sowinski, A., Mehrani, P., and Passalacqua, A. (2018). *An Euler-Euler model for mono-dispersed gas-particle flows incorporating electrostatic charging due to particle-wall and particle-particle collisions*. Chem. Eng. Sci., 197:327–344.

[118] Villafañe, L., Banko, A., Elkins, C., and Eaton, J. K. (2017). *Gas heating by radiation absorbing inertial particles in a turbulent duct flow*. In *Annual Research Briefs*. Center for Turbulence Research, Stanford University, USA.

[119] pafiX (2019). `http://www.ptb.de/cms/asep`.

https://doi.org/10.7795/110.20221208

A. Author contribution statement

The authors contribution to the publications summarized in this document which have several authors is as follows.

[1] **H. Grosshans**, M. Griesing, M. Mönckedieck, T. Hellwig, B. Walther, S.R. Gopireddy, W. Pauer, H.-U. Moritz, N. Urbanetz, and E. Gutheil, *Numerical and experimental study of the drying of bi-component droplets under various drying conditions*, International Journal of Heat and Mass Transfer, 96, 97–109, May 2016

For this study I modified the single droplet drying code which has previously been developed in the group of Prof. Dr. E. Gutheil (Heidelberg University). I performed all simulations and post-processed the results. The experiments and the design of experiment were conducted by the respective groups at Hamburg University, Graz University of Technology and Kiel University. The writing was a joint effort by all authors.

[2] **H. Grosshans**, M. Griesing, T. Hellwig, W. Pauer, H.-U. Moritz, and E. Gutheil, *A new model for the drying of mannitol-water droplets in hot air above the boiling temperature*, Powder Technology, 297, 259–265, April 2016

I developed the new mathematical model and implemented it in the single droplet drying code which has previously been developed in the group of Prof. Dr. E. Gutheil (Heidelberg University). I performed all simulations and post-processed the results. The experiments were conducted by the group at Hamburg University. The manuscripts was mostly written by me with contributions by all authors.

[3] **H. Grosshans**, S.R. Gopireddy, and E. Gutheil, *Numerical simulation of PVP-water sprays under various injection conditions*, 26th European Conference on Liquid Atomization and Spray Systems, ILASS – Europe 2014, September 8–10, 2014, Bremen, Germany

I implemented the approach to establish initial conditions for the DQMOM simulations from experimental data. I performed all simulations using the DQMOM code which has previously been developed in the group of Prof. Dr. E. Gutheil (Heidelberg University) and post-processed the results. The manuscripts was mostly written by me with contributions by all authors.

[4] **H. Grosshans**, S.R. Gopireddy, R.M. Humza, and E. Gutheil, *Modeling and simulation of single particle and spray drying of PVP- and mannitol-water in hot air*, in: Process-Spray: Functional Particles Produced in Spray Processes, Springer Science & Business Media, Springer, June 2016

I extended the DQMOM formulation to account for temperature changes and implemented the coupling of the code to OpenFOAM. Also, the paper summarizes numerical work which was previously performed by the co-authors. The writing was a joint effort by all authors.

[5] **H. Grosshans** and M.V. Papalexandris, *A model for the non-uniform contact charging of particles*, Powder Technology, 305, 518–527, January 2017

I implemented the numerical methodology and performed the simulations. My co-author contributed to the interpretation of the resulting data and the writing of the manuscript.

https://doi.org/10.7795/110.20221208

[6] **H. Grosshans** and M.V. Papalexandris, *Direct numerical simulation of the triboelectric charging in particle-laden turbulent channel flows*, Journal of Fluid Mechanics, 818, 465–491, March 2017

I implemented the numerical methodology and performed the simulations. My co-author contributed to the interpretation of the resulting data and the writing of the manuscript.

[7] **H. Grosshans** and M.V. Papalexandris, *Exploring the mechanism of inter-particle charge diffusion*, European Physical Journal Applied Physics, 82(1), 11101, 2018

I implemented the numerical methodology and performed the simulations. My co-author contributed to the interpretation of the resulting data and the writing of the manuscript.

[8] **H. Grosshans** and M.V. Papalexandris, *Large eddy simulation of triboelectric charging in pneumatic powder transport*, Powder Technology, 301, 1008–1015, July 2016

I implemented the numerical methodology and performed the simulations. My co-author contributed to the interpretation of the resulting data and the writing of the manuscript.

[9] **H. Grosshans** and M.V. Papalexandris, *Evaluation of the parameters influencing electrostatic charging of powder in a pipe flow*, Journal of Loss Prevention in the Process Industries, 43, 83–91, May 2016

I implemented the numerical methodology and performed the simulations. My co-author contributed to the interpretation of the resulting data and the writing of the manuscript.

[10] **H. Grosshans** and M.V. Papalexandris, *Numerical study of the influence of the powder and pipe properties on electrical charging during pneumatic conveying*, Powder Technology, 315, 227–235, April 2017

I implemented the numerical methodology and performed the simulations. My co-author contributed to the interpretation of the resulting data and the writing of the manuscript.

[11] N. Schwindt, U. von Pidoll, D. Markus, U. Klausmeyer, M.V. Papalexandris, and **H. Grosshans**, *Measurement of electrostatic charging during pneumatic conveying of powders*, Journal of Loss Prevention in the Process Industries, 49, 461–471, June 2017

The experiment was set up and all experiments were conducted by N. Schwindt under the guidance of Dr. U. von Pidoll, Dr. D. Markus, Prof. Dr. U. Klausmeyer, and me. I performed the corresponding simulations. The manuscripts was mostly written by me with contributions by all authors.

[12] **H. Grosshans**, R.-Z. Szász, and M.V. Papalexandris, *Modeling the electrostatic charging of a helicopter during hovering flight in dusty atmosphere*, Aerospace Science and Technology, 64, 31–38, January 2017

The code was jointly developed by Dr. R.-Z. Szász and me. I performed all the simulations and post-processed the results. My co-authors contributed to the interpretation of the data and the writing of the manuscript.

[13] **H. Grosshans**, R.-Z. Szász, and M.V. Papalexandris, *Influence of the rotor configuration on the electrostatic charging of helicopters*, AIAA Journal, 56(1), 368–375, January 2018

The code was jointly developed by Dr. R.-Z. Szász and me. I performed all the simulations and post-processed the results. My co-authors contributed to the interpretation of the data and the writing of the manuscript.

[14] **H. Grosshans** and M.V. Papalexandris, *On the accuracy of the numerical computation of the electrostatic forces between charged particles*, Powder Technology, 322, 185–194, September 2017

https://doi.org/10.7795/110.20221208

I implemented the numerical methodology and performed the simulations. My co-author contributed to the interpretation of the resulting data and the writing of the manuscript.

[15] **H. Grosshans**, L. Villafañe, A. Banko, and M.V. Papalexandris, Case study on the influence of electrostatic charges on particle concentration in turbulent duct flows, *Powder Technology*, 357, 46–53, September 2019

The experiment was set up and all experiments were conducted by the group at Stanford University. I implemented the numerical methodology and performed the corresponding simulations. The manuscript was mostly written by me with contributions by all authors.

https://doi.org/10.7795/110.20221208

B. Acknowledgments

The financial support through the following organizations and grants is gratefully acknowledged:

- Deutsche Forschungsgemeinschaft (SPP 1423)
- National Research Fund of Belgium (GRANMIX Projet de Recherche grant)
- Max Buchner Research Foundation (grant no. 3680 and 3736)

https://doi.org/10.7795/110.20221208

C. Curriculum Vitae

Personal information

Name	Holger Grosshans
Date of birth	21.10.1978
Place of birth	Speyer, Germany

Current position

from 7/2017	Physikalisch-Technische Bundesanstalt, Braunschweig, Germany Head of the group “Analysis & Simulation in Explosion Protection”
from 10/2018	University of Magdeburg, Germany Lecturer in the “Institute of Apparatus- and Environmental Technology”

Education

27.3.2013	Ph.D. degree, Lund University, Sweden, supervisor: Prof. László Fuchs
5.11.2007	Diplom-Ingenieur (Master of Engineering) in Aerospace Engineering, Technical University of Dresden, Germany
6.12.2002	Bachelor of Science, The Open University, UK
30.9.2002	Diplom-Ingenieur (BA), Baden-Württemberg Cooperative State University Ravensburg, Germany

Professional experience

4/2019–6/2019	Soka University, Tokyo, Japan Guest researcher in the group of Prof. Tatsushi Matsuyama
10/2015–6/2017	Université Catholique de Louvain, Louvain-la-Neuve, Belgium Post-doctoral researcher in the group of Prof. Miltiadis V. Papalexandris
10/2013–9/2015	Heidelberg University, Germany Post-doctoral researcher in the group of Prof. Eva Gutheil
12/2008–6/2013	Lund University, Sweden Researcher in the group of Prof. László Fuchs
9/1999–8/2008	Airbus, Bremen/Hamburg/Munich, Germany Flight Physics and System Design department

https://doi.org/10.7795/110.20221208

Herausgeber:
Physikalisch-Technische Bundesanstalt
ISNI: 0000 0001 2186 1887

Presse und Öffentlichkeitsarbeit

Bundesallee 100
38116 Braunschweig

Telefon: (05 31) 592-93 21
Telefax: (05 31) 592-92 92
www.ptb.de

Vertrieb:
Fachverlag NW in der
Carl Schünemann Verlag GmbH

Zweite Schlachtpforte 7
28195 Bremen

Telefon: (04 21) 369 03-0
Telefax: (04 21) 369 03-63
www.schuenemann-verlag.de